EUROPEAN ORGANIZATION FOR NUCLEAR RESEARCH

SIGRUM

A SUPERCONDUCTING ION GANTRY WITH RIBONI'S UNCONVENTIONAL MECHANICS

U. Amaldi, N. Alharbi, E. Benedetto[1], P.L. Riboni and M. Vaziri

TERA Foundation

D. Aguglia, V. Ferrentino, G. Le Godec, M. Karppinen, D. Perini, E. Ravaioli and D. Tommasini

CERN

[1]   At present CERN Project Associate

SIGRUM
A **S**uperconducting **I**on **G**antry with **R**iboni's **U**nconventional **Mechanics**

U. Amaldi, N. Alharbi, E. Benedetto,[1] P.L. Riboni and M. Vaziri

TERA Foundation

D. Aguglia, V.Ferrentino, G. Le Godec, M.Karppinen, D. Perini, E.Ravaioli and D. Tommasini

CERN

IN MEMORY OF PIERLUIGI RIBONI

1. Introduction

This report describes the conceptual design of a 430 MeV/u carbon ion gantry that is based on superconducting (SC) magnets and features a novel mechanical support. This gantry is at least ten times lighter than the ones existing at present.

Two different configurations have been studied, a first one based on superconducting canted cosine-theta magnets operating at 4 T, and a second one based on superconducting cosine-theta magnets operating at 3 T. The second configuration, though less compact than the first one, makes use of already consolidated technologies developed at CERN on accelerator magnets and should allow the manufacture and installation of such a gantry with minimal R&D effort, within less than one decade.

The first ion gantry ever built is based on *normal temperature* magnets and has been designed by GSI (Darmstadt) for the proton and carbon ion centre HIT (Heidelberg); it weighs 600 tons[2]. Obviously *superconducting magnets* are very advantageous in the constructions of ion gantries, which are large and expensive because 430 MeV/u carbon ions have a large rigidity: 6.6 Tm. A collaboration among NIRS, KEK and Toshiba scientists and engineers, who designed and built the gantry shown if Figure 1, which has a 6 m external diameter and weighs 300 tons[3].
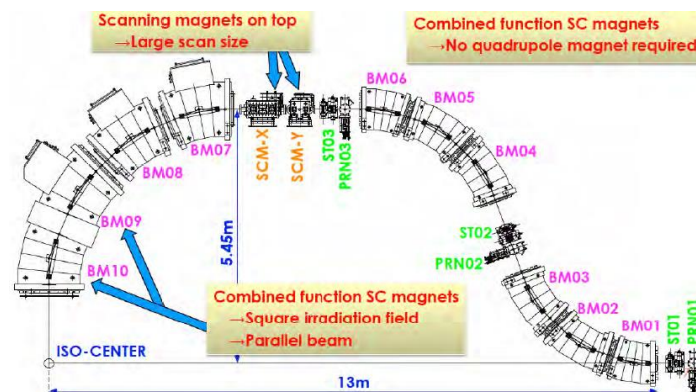

Figure 1. *The NIRS 430 MeV/u carbon ion gantry has a 20 cm x 20 cm irradiation field.*

---

[1] At present CERN Project Associate.

[2] U. Weinrich and CM Kleffner, *Commissioning of the Carbon Beam Gantry of the Heidelberg Ion Therapy (HIT)*, 11th Eu Part Acc Conf, Genoa, June 2008, pp. TUPP134.

[3] Y. Iwata et al, *Development of a superconducting rotating-gantry for heavy-ion therapy*, J Radiat Res, 55 – Suppl 1 (2014): i24–i25; doi: 10.1093/irr/rrt205

As indicated in the figure, the last bending system is made of 4 combined function dipoles of the cosine-theta type and the Scanning Magnets, which move the beam on the x-y treatment area and are *upstream* of this system. This choice requires large apertures but has the advantage of producing large Source Axis Distances (SADs).

In the most recent design by NIRS shown in Figure 2, the scanning magnet are *downstream* of the last bending magnet, which has a small aperture. As a consequence, the SADs are relatively small - about 2.0 and 2.3 m – but the gantry, based on 90° bending magnets, is definitely more compact[4].
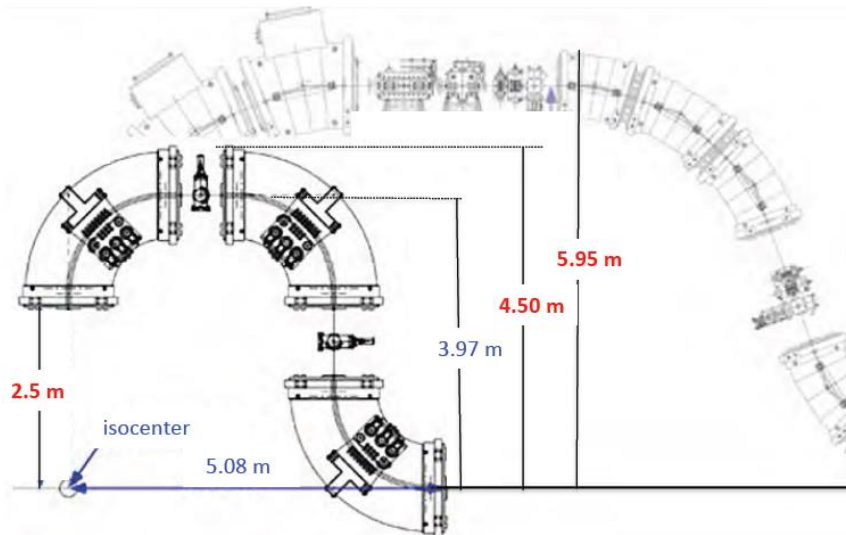

Figure 2. *The recent compact design by NIRS, with a 4.5 m external radius, is compared with the one of Figure 1.*

Any new carbon ion gantry design has to be compared with the designs of Figure 1 and 2, which use 2.9 T and 5 T SC bending magnets, respectively.

2. The light ion gantry with 4 T canted cosine-theta magnets

In the years 2015-2017, in the framework of TERA activities, P.L. R. and M.V. designed the mechanics of a light (35 tons) *room temperature proton* gantry without counterweight and attached to the wall of the treatment room. At the end of 2017 one of us (U.A.) studied a *superconducting carbon ion* gantry, using the support proposed for the proton gantry, and of a synchrotron, based on the same 2-magnet/1-quadrupole bending system, as shown in Figure 3[5].

For the synchrotron an ion injector linac having a small emittance was chosen so that enough carbon ions could be injected and accelerate to treat a 1-litre tumour in a *single* accelerator cycle.

For the 430 MeV/u carbon ion gantry the bending field was chosen to be 4.0 T so that the gantry radius was 5.3 metres, as shown in Figure 3. In the following months the mechanics of the new superconducting gantry was designed by of two of us (P.L. R. and N.A), by applying

[4] J.B. Farr, J.B. Flanz, A Gerbershagen, M.F. Moyers, *New horizons in particle therapy systems*, Med Phys, 13 November 2018, https://doi.org/10.1002/mp.1319

[5] U. Amaldi, *A "Slow" Superconducting Synchrotron and Gantry for Carbon Ion Therapy,* TERA Note – 28/12/17.

the same principles used in the design of the normal conducting proton gantry mentioned above.
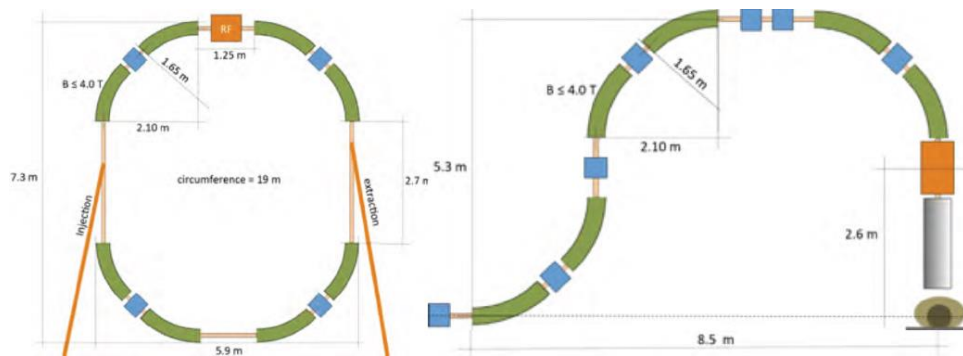

Figure 3. *2017 proposal of a 430 MeV/u carbon ion synchrotron and a gantry, which are based on 45° SC 4-tesla bending magnets (radius of curvature = 1.65 m radius). The average SAD, which is the distance from the 'Source' of the scanning beams to the 'Axis', is 2.6 m.*

In parallel, a collaboration was established with G. Arduini and D. Tommasini to define the parameters of the synchrotron and the gantry. In April 2018 one of us (E.B.) joined TERA and initiated the design of the synchrotron and gantry optics. In May one of us (D. T.) proposed the use of SC *Alternating-Gradient Canted Cosine Theta* magnets (AG-CCT)[6]. This option was discussed with members of the LBNL group and a collaboration was established with S. Prestemon and L. Brouwer, who calculated with their software the magnets. These are 90^0 NbTi magnets and have two inner layers of Alternating Gradient quadrupole windings and an outer set of dipole layers to generate the desired fields, following directly from their previous LBNL work.

The gantry is schematically shown in Figure 4a together with the rotating structure (Figure 4b), which has been dimensioned such that it distorts by less than 1 mm while the gantry is at any angle between +110° and -110° with respect to the horizontal plane.
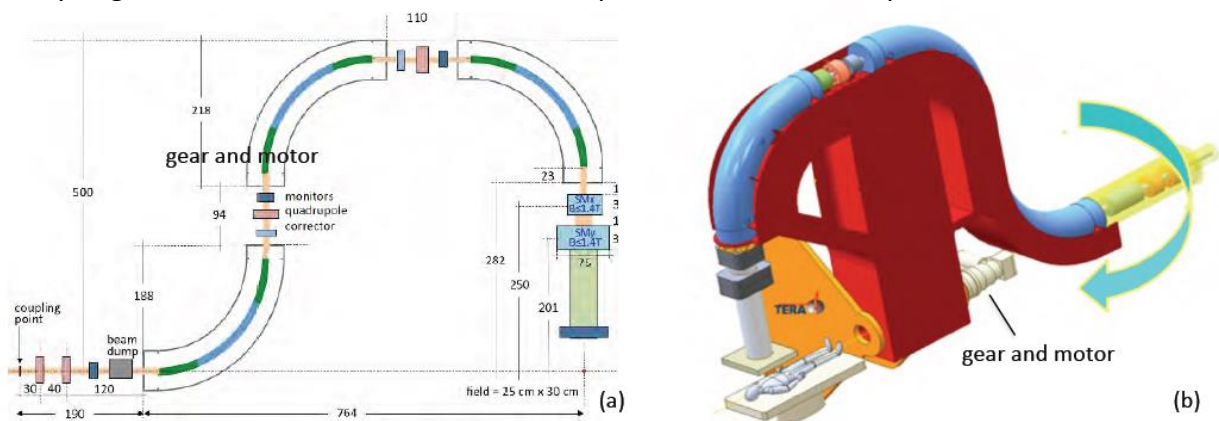

Figure 4. *Layout of the 2018 version of the 4 T gantry. Three quadrupoles (coloured in green and blue) are superimposed to the bending magnets of the three 90° magnets ('nested-quadrupoles'). The cables are in NbTi and the magnets weight 4 tons.*

---

[6] W. Wan, L. Brouwer, S. Caspi, S. Prestemon, A. Gerbershagen, J. M. Schippers and D. Robin, *Alternating-gradient canted cosine theta superconducting magnets for future compact proton gantrie*s, Phys. Rev. ST Accel. Beams 18, 103501 – Published 23 October 2015.

The rotating part of the gantry weighs 33 tons and can be transported as a *single piece from the construction and testing workshop to the therapy centre*. The support, attached to the wall, weighs about 15 tons*.

The principles driving the design of the gantry mechanics have been simplification and compactness. Simplification means – by using the 'Occam Razor' - removing all the mechanical structures that are not functional to the beam transport.

The gantry is rotated by a special gear-motor system (Figure 5) that is powerful enough so that the gantry does not need a counterweight. This choice, in itself, reduces the weight and the space occupied by the gantry by about a factor two.
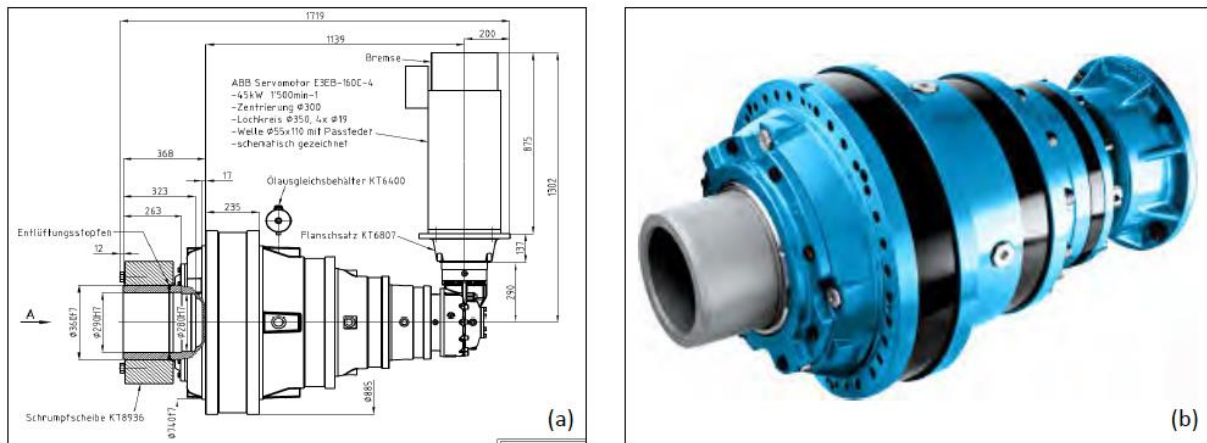

Figure 5. *(a) The epicycloidal gear is a standard industrial product. (b) A gear by the company Brevini is shown as an example.*

A further very important simplification, with a consequent weight reduction, has been introduced by using the magnets of the beam line as part of the mechanical structure, thus increasing the overall rigidity of the system.

Another simplification has been obtained by attaching the gantry to the wall of the treatment room and by allowing a rotation of $\pm 110^0$ (which is enough for most of the treatment plans[7], and even for all of them if the patient bed is rotated by 180^0). All these simplifications ultimately lead to compactness.

The rotation by $\pm 110^0$ is driven by an electric motor with a high-torque planetary gear, which moves precisely the gantry to any angular position. Finite element analyses show that all distortions - with the gantry in any position between +110° and -110° - are smaller than 1 mm.

At present a paper is being completed for submission to *Physics in Medicine and Biology*:
E. Benedetto, N. Al Harbi, L. Brouwer, S. Prestemon, P. Riboni, D. Tommasini and U. Amaldi, *"A carbon ion superconducting gantry and a synchrotron based on Canted Cosine Theta magnets"*.

---

[7] S. Yan, H.M. Lu, J. Flanz, J. Adams, A. Trofimov and T. Bortfeld, *Reassessment of the Necessity of the Proton Gantry: Analysis of Beam Orientations From 4332 Treatments at the Massachusetts General Hospital Proton Center Over the Past 10 Years*, Int J Radiat Oncol Biol Phys 95 (2016) 224-233.

3. Dose delivery

In November 2019 CNAO and MedAustron expressed interest in collaborating with CERN and TERA on the design of the carbon ion gantry, whose construction should start in 2023. This request has motivated the study of a *more conservative option* for the superconducting magnets than the one of Fig. 4, making the best use of the CERN experience, to reduce the required R&D within acceptable terms with respect to the timeline of the project. The conservatively lower bending field (3 T instead than 4 T) *unavoidably* implies a larger external radius.

Before discussing the properties of the 3 T gantry, this Section describes the dose delivery procedure and its timing using the CNAO preferred parameters as inputs. *The results are used in Section 4 to define the parameters of the 3-tesla gantry.*

The momentum of the ion beam, sent to the SC gantry, is schematically shown in Figure 6 as a function of time.
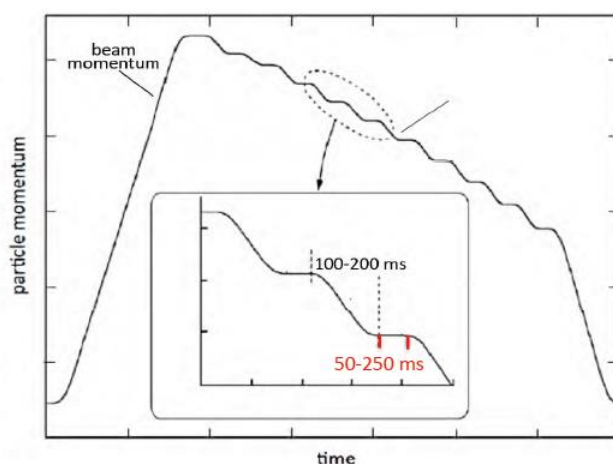

Figure 6. *Time dependence of the ion beam momentum. In CNAO the number of flat-tops M_F in a synchrotron cycle will be small: M_F = 1-8.*

Following the work done at NIRS [8], to obtain such a stepwise behaviour the carbon ion beam is extracted from the synchrotron by RF knock-out in many mini-flat-tops of decreasing (increasing, if preferred) momentum. During each one of these M_F mini-flat-tops, the Bragg spot is moved in x and y to scan one full layer of the tumour target. The typical time for changing energy is 100-200 ms, as indicated in the figure, and the duration of each flat top varies according to the number of carbon ions that have to be sent to the many planned spots of the visited layer. As mentioned in the figure caption, at CNAO M_F will be small but in the future SC ion synchrotrons M_F may go up to 50-60 with a reduction of the treatment times. In some circumstances at CNAO it may be necessary to have M_F= 1 and even scan the same target layer during two flat-tops that may even belong to different synchrotron cycles.

In this Section, as irradiation examples, two 1-litre water targets (radius r = 62.0 mm) are considered with centres at water-depths R = 250 mm and R = 100 mm. Each target is subdivided longitudinally in N_L 'layers' with N_L = 2 r / ΔR_L = 62, where ΔR_L = 2.0 mm is the layer thickness presently used at CNAO.

---

[8] Y. Iwata, T. Kadowaki, H. Uchiyam et al, *Multiple-energy operation with extended flattops at HIMAC*, Nucl Instr Meth A 624 (2010) 33-38.

In the following, to pass from the carbon beam energy $E_{MeV/u}$ to the water-range i R_{mm}, and viceversa, two approximate relations will be used

$$E_{MeV/u} = 15.12\ R_{mm}^{0.581} \quad \text{and} \quad R_{mm} = 0.0094\ E_{MeV/u}^{1.72} \tag{1}$$

so that

$$\frac{\Delta R}{R} = 1.72\ \frac{\Delta E}{E} = 1.72\ \frac{\gamma+1}{\gamma}\frac{\Delta p}{p} \quad \text{and} \quad \Delta R/R \cong 3\ \Delta p/p. \tag{2}$$

The last, very important relation says that, with

$$\textbf{Δp/p = ±1\%}, \tag{3}$$

and an R = 200 mm water-depth, the range variation is about ±6 mm. These 12 mm are equal to 3-6 longitudinally scanned layers – which are, typically, 2-4 mm thick – and sufficient to follow a moving target *without changing* the magnet currents.

3.1. Transverse (x-y) scanning

In the transverse plane the voxel area is determined by the total width of the carbon ion Bragg spot, which is the quadratic combination of the Full Width Half Maximum due to the beam dimensions at the isocentre *without patient* ('in air') $FWHM_{be}$ and the width due to multiple scattering in the target $FWHM_{ms}$:

$$FWHM_{spot} = (FWHM_{ms}^2 + FWHM_{be}^2)^{1/2} \tag{4}$$

The depth dependence of the multiple scattering transverse sigma is plotted in Figure 7 for various light ions.
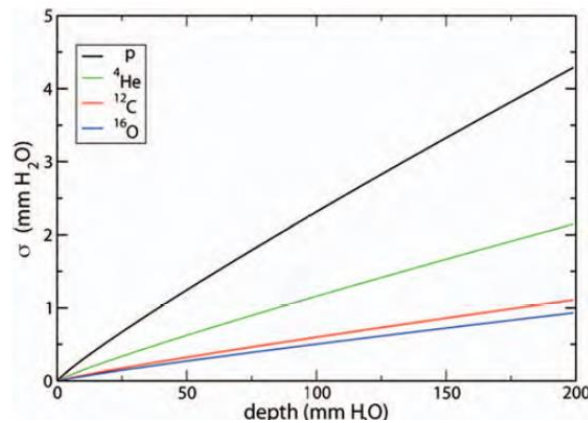

Figure 7. *Depth dependence of the sigma of the two transverse distributions of the Bragg spot[9].*

The figure shows that, for carbon ions, the Full Width at Half Maximum due to multiple scattering can be written in the form

$$FWHM_{ms} \cong 0.048\ A^{-1/2}\ R_{mm}. \tag{5}$$

By using Eq. (4) the values computed for the two 1-litre targets are listed in column 4 of Table 3. The minimum value is 4.35 mm at 430 MeV/u.

In all hadron therapy centres the beam width is adjusted in the interval 4.0-10 mm according to the dimensions of the target and the vicinity of Organ At Risk (OARs). At CNAO the values

---

[9] Ref.4.

$FWHM_{be}$ = 4.0 mm and $FWHM_{be}$ = 8.0 mm are typically used respectively for distal (R =320 mm) and proximal (R = 25 mm) depositions.

As shown in the first and last row of column 6, $FWHM_{be}$ = 4.0 mm and $FWHM_{be}$ = 8.0 give spot widths $FWHM_{spot}$ that are 6.0 mm and 8 .0 mm. As indicated in the central rows of column (6), by choosing - for scanning each one of the 1-litre targets - a fixed value of the beam width $FWHM_{be}$ (i.e. 5.0 mm and 8.0 mm respectively) the combined widths $FWHM_{spots}$ vary in narrow ranges: (6.1 ± 0.5) mm and (8.15 ± 0.15) mm. These ±9% and ±2% variations of the spot width are small and, thus, it is not necessary to adjust the beam width $FWHM_{be}$ during a treatment- even when the scanned targets are large.

Table 3. *Beam parameters in the treatment of two spherical 1-litre water volumes (radius = 62 smm)placed at 250 mm and 100 mm water depths.*

	(1)	(2)	(3)	(4)	(5)	(6)	(7)
	Range R mm	Energy [a] MeV/u	Momentum (GeV/c)/Z	$FWHM_{ms}$ [b] mm	$FWHM_{be}$ mm	$FWHM_{spot}$ [c] mm	$FWHM_{straggling}$ [d] mm
	318	**430**	1.986	4.40	4.0	**5.95**	**2.20**
T A R G 1	312	**425**	1.966	4.35	5.0	6.6	**2.15**
	250	**374**	1.827	3.45	5.0	6.1	**1.75**
	188	**317**	1.661	2.60	5.0	5.6	**1.30**
T A R G 2	162	**291**	1.731	2.25	8.0	8.3	**1.10**
	100	**220**	1.353	1.40	8.0	8.1	**0.70**
	38	**125**	997	0.52	8.0	8.0	**0.25**
	26	**100**	886	0.35	8.0	**8.0**	**0.18**

[a] From Eq. 1.   [b] From Eq. 5.   [c] From Eq. 4.   [d] From Eq. 6.

3.2   Longitudinal (z) scanning

The longitudinal width σ of the Bragg peak, due to ions *straggling*, is *shown* in Figure 8 [10], which h shows that the Full Width at Half Maximum due to straggling $FWHM_{st} \approx 2.4\ \sigma$ is roughly proportional to the range and inversely proportional to $A^{1/2}$ and it can be written as

$$FWHM_{straggling} \cong 0.024\ A^{-1/2} R_{mm}. \quad \text{(mono-energetic beam).} \tag{6}$$

The approximate values of $FWHM_{straggling}$ are listed in Column 7 of Table 3. (It is worthwhile noting that the constant 0.024 is half the value of the constant appearing in Eq. 5.)

Typically, the 'layer' thickness - i.e., the thickness of an 'iso-energetic slice' of the target - is in the range 2-5 mm, smaller than the $FWHM_{straggling}$ of a monoenergetic ion beam (Eq. 5 and Figure 9a). To get a uniformly distributed longitudinal dose the momentum spread of the beam has to be increased either by acting on the accelerator or by placing along the transport line a 'ridge filter' or two (Figure 9b). It has to be noted that many narrow peaks have to be summed up in order to obtain a Spread Out Bragg Peak (Figure 10).
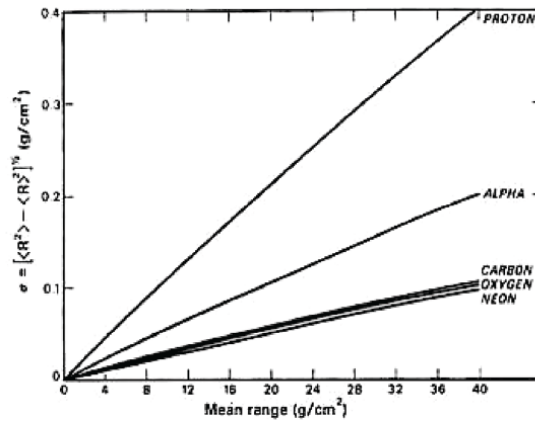
---

[10] *Dose reporting of ions beams,* IEEA-TECDOC-1560

Figure 8. *The range dispersion σ is roughly proportional to the range R.*
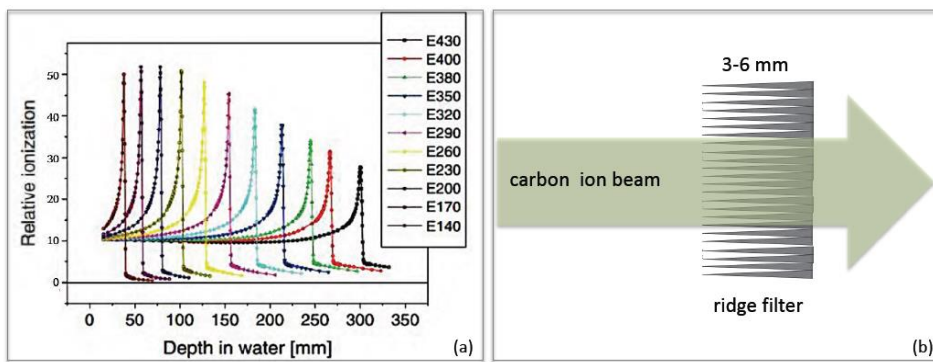

Figure 9. *(a) Longitudinal distributions of the carbon ion dose; the peak height decreases with the depth because the carbon ions fragment due to nuclear interactions. (b) Sketch of a ridge filter.*
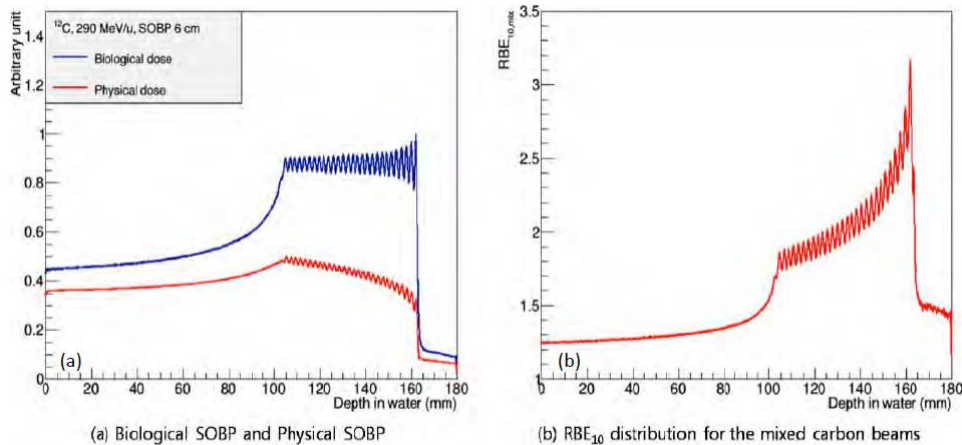

(a) Biological SOBP and Physical SOBP

(b) RBE$_{10}$ distribution for the mixed carbon beams

Figure 10. *Depth distributions (a) of the physical (red) and of the 'effective' (blue) doses and (b) of the Radio Biological Effectiveness (RBE)* [11]. *The (physical) dose is measured in grays (1 Gy = 1 J/kg) and the effective dose in Gy(RBE).*

Since, as shown in Figure 10b, the Radio Biological Effectiveness (RBE) increases at the end of the ion range, (where the ionization density is larger) to obtain a longitudinally uniform *effective* dose (blue curve of Figure 10a), the (physical) dose has to decrease with the depth

---

[11] The RBE of Figure 10 corresponds to a 10% survival rate of human salivary gland cells: Cho, I. et al., Journal of the Korean Physical Society, 69 (2016) 868–874. https://doi.org/10.3938/jkps.69.868

(red curve). The figure illustrates the case of a 60 mm target, with its centre placed at 130 mm from the surface, covered by N_L = 30 layers with a ΔR_L = 2.0 mm thickness. The zigzags of the red and blue lines are due to the fact that the width of Eq. 6 ($FWHM_{straggling} \approx$ 0.9 mm at R = 130 mm) is too small with respect to ΔR_L, an effect that can be reduced with a proper ridge filter.

During the treatments of the two 1-litre targets the fields of the gantry magnets have to be varied as shown in column (5) of Table 4.

Table 4. *Beam parameters in the treatment of two spherical 1-litre water volumes placed at 250 mm and 100 mm water depths.*

	(1) Range *R* mm	(2) Momentum ([a]) (GeV/c)/Z	(3) Rigidity T m	(4) B-field T	(5) % differ.	(6) ΔR_L mm	(7) ΔB ([b]) mT	(8) ΔT ([c]) ms
	318	1.986	6.625	**3.00**				
T A R G 1	312	1.966	6.558	**2.97**	+ 7.2 %		12.7	127
	250	1.827	6.094	**2.77**	-	4.0	14.9	148
	188	1.661	5.541	**2.51**	- 9.4%		17.8	178
T A R G 2	162	1.731	5.774	**2.61**	+ 28%		10.7	107
	100	1.353	4.513	**2.04**	-	2.0	13.6	136
	38	997	3.392	**1.54**	- 30%		20.3	203
	26	886	2.956	**1.34**				

([a]) From column 3 of Table 3.
([b]) ΔB is computed introducing, for the two targets, ΔR_L = 4.0 mm and ΔR_L = 2.0 mm in Eq. (3): $\Delta B/B = \Delta R/3R$.
([c]) The time ΔT to change layer is computed from column (7) with a $\Delta B/\Delta t$ = 0.1 T/s field rate as in Eq. (8).

Column (6) shows that, if the beam and gantry transport lines had a very large momentum acceptance ($\Delta p/p \approx \pm$ 15%), even for very small depths, the irradiation of a target that is $\pm$ 60 mm thick at 250 mm (and $\pm$ 30 mm thick at 100 mm) can be done very rapidly *without varying* the magnetic fields. With this goal in mind many groups are developing SC magnetic systems with such larger acceptances, which by necessity - for carbon ions - are very large and expensive. To move rapidly towards the construction of the gantry described in this Report, the choice has been made to have a large enough aperture to obtain $\Delta p/p = \pm$ 1% (Eq. 3), but no more, so that several layers can be irradiate without changing the magnetic field. According to Eq. 2, this choice implies $\Delta R/R = \pm$ 3.0%, i.e. - on average - $\Delta R = \pm 7.5$ mm and $\Delta R = \pm 3.0$ mm for targets located around R = 250 mm and R = 100 mm. With ΔR_L = 2.0 mm, this implies that 7 and 3 layers can be irradiated, respectively, *without changing* the gantry magnetic field.

For the two 124 mm diameter spherical targets of Tables 3 and 4 two layer thicknesses have been chosen in column (6): ΔR_L = 4.0 mm and ΔR_L = 2.0 mm. The entries of column (9) show that the jumps of the magnetic fields are in the range 10-20 mT.

To keep the cryogenic losses to a minimum it has been decided to *drastically* limit the rate of variation of the fields in the gantry bending magnet:

$$\Delta B/\Delta t \leqq 0.10 \text{ T/s} \qquad \text{(bending magnets)} \qquad (7)$$

Column 8 of Table 4, computed with $\Delta B/\Delta t = 0.10$ T/s, shows that 150 ms is the typical time to pass from one layer to the next, to which 100 ms of setting time have to be added.

3.3 Dose delivery and its timing

The quantities defining the two treatment examples are collected in Table 5.

Table 5. Parameter of dose delivery for the two targets of Tables 3 and 4.

Quantity	Unit	1-litre target (250 mm)	1-litre target (100 mm)
1. Spot Full Width at Half Maximum $FWHM_{spot}$	mm	6.0	8.0
2. Transverse step $\Delta x = \Delta y = FWHM_{spot}/3$	mm	**2.0**	**2.7**
3. Layer thickness ΔR_L	mm	**4.0**	**2.0**
4. Voxel volume $\Delta V = \Delta x \ \Delta y \ \Delta R_L$	mm^3	16.0	14.2
5. Number of voxels $N_V = 10^6$ mm^3/V		62,500	70,500
6. Number of layers $L = 124$ mm$/\Delta R_L$		31	62
7. Average layer changing time t_L (^{a})	ms	280	250
8. Total **layer changing time** $T_L = (L-1) \ t_L$ (^{b})	s	**8.4**	**15.5**
9. Speed to move in x or y from one spot to the next v_{spot}	m/s	**20**	**20**
10. Time to move from a spot to the next $t_M = \Delta x / v_{spot}$	ms	0.10	0.10
11. Total **spot moving time** $T_M = N_V t_M$ (^{c})	s	**6.3**	**7.1**
12. Sum of layer changing and spot moving times $(T_L + T_M)$	s	14.7	22.5
13. Average delivery time per spot $t_{av.del}$ (interval 0.5-6 ms)	ms	2.0	2.0
14. Total **irradiation time** $T_I = N_V t_{av.del}$	s	**125**	**141**
15. Total **treatment time** in a synchrotron cycle $T_T = (T_L + T_M + T_I)$	s	**140**	**164**
16. Average number M_F of flat-tops per synchrotron cycle (^{d})		4	4
17. Extra time for $N_F = L \ t_c \ / \ M_F$ synchrotron cycles ($t_c = 1.5$ s)	s	**12**	**24**
18. Total **treatment time** in N_F synchrotron cycles: 15 + 17	s	<u>**152**</u>	<u>**188**</u>

(^{a}) 100 ms have been added to the maximum numbers appearing in column (8) of Table 4.
(^{b}) This is valid if the M_F flat-tops belong to a single synchrotron cycle. If this is not the case the time to be added is computed in rows 17.
(^{c}) This is an upper limit because for many targets some of the N_V voxels require zero dose and shave not to be visited by the beam spot.
(^{d}) This requires an upgrade of the present CNAO control system o that M_F can be chosen in the range 1-8 with 4 as an average number.

The starting point is the transverse step that, in the *raster scanning* procedure used at HIT and CNAO, is **one third** of $FWHM_{spot}$ (row 2). The spot velocity (for relatively long displacements) is given in row 9:

$$v_{spot} = 20 \text{ m/s} = 20 \text{ mm/ms,} \qquad (8)$$

and the time to move from one voxel (whose centre coincides with the centre of the 'planned spot') to the next is (row 10):

$$t_M = 0.10 \text{ ms}. \tag{9}$$

Since this duration is not much longer than the typical switching and stabilization times, for $\Delta x = \Delta y$ = 2-3 mm the *instantaneous* spot velocity has to be larger than the one of Eq. (8). This is challenging from the point of view of the power supplies.

The average time, spent to irradiate a planned spot, has to be definitely larger than t_M; in row 13 the choice has been made that the ratio between these two times is 20:

$$t_{av \cdot del} = 2.0 \text{ ms/spot} \tag{10}$$

with a variability in the approximate range 0.5-6.0 ms/spot, as indicated in the same row.

With this choice, if the ion current is not switched off but kept roughly constant during the treatment of a line of voxels, the delivery time of each spot is proportional to the dose to be delivered and, during the spot movements, the transverse segments $\Delta x, \Delta y$ = 2-3 mm (row 2) are irradiated with a number of ions that is, on average, 20 times smaller than the one that irradiates the contiguous planned spots. This effect of about 5% has to be considered by the Treatment Planning System (TPS).

To conclude this Section, it is interesting to estimate the number of ions needed to give a 2 Gy physical dose (1 gray =1 J/kg) to the 1-litre targets.

The TPS defines the number of carbon ions to be directed to each voxel (or planned spot) so that the dose multiplied by the relevant RBE is uniform on the whole1-litre volume (see Figure 8a). Because of the ion traversing the first target layers, the numbers of carbon ions directed to the planned spots of the proximal layers are smaller than the ones directed to the distal layers. The number of carbon ions can be estimated by observing that, when irradiated uniformly on a spherical target, most of the ions reach the distal layers and thus have a range definitely *larger* than the sphere radius, which in the two examples is r = 62 mm. Assuming an *average* range R_{av} = 80 mm, a carbon ion leaves in the target an energy $A\, E_{MeV/u} = 15.12\, A\, R_{av}^{0.581}$ = 2300 MeV, i.e. 3.7 10^{-10} J. To deliver 2 J to 1 kg of water - with an overall extraction and treatment efficiency equal to 50 % - about 10^{10} carbon ions are needed.

Figure 16b shows that, at the centre of a Spread-Out Bragg Peak, the typical RBE is equal to 2, so that a 2 Gy physical dose corresponds, on average, to a 4 Gy(RBE) effective dose. Since the typical irradiation of the two 1-litre targets lasts about 2 minutes (row 15 of Table 5), overall, the standard rate of conventional radiotherapy "2 Gy(RBE) per litre per minute" is reached.

4. The light ion gantry with 3 T cosine-theta magnets

4.1 Main parameters

The list of parameters contains 11 main points:
1. the maximum bending field is 3.0 T - Column 4 of Table 4;
2. the magnets are combined function with gradients smaller than 5 T/m and a fixed ratio between the quadrupole and the dipole fields;
3. the diameter of the vacuum chamber is 60 mm;
4. the aperture of the coils is 70 mm;
5. the radius of the gantry can be as large as 6.5 m;

6. the momentum acceptance is relatively large: $\Delta p/p = \pm 1\%$ – Eq. (3);
7. the FWHM of the ion beam at the isocentre can be chosen in the range 4-8 mm;
8. the ramping speed of the bending magnets is not greater than 0.1 T/s – Eq. (7) ;
9. the scanning speed is a*t least* 20 m/s – Eq. (8) – so that the beam spot can move by 2 mm in 0.1 ms – a challenging requirement as stated after Eq. (9);
10. the maximum SAD of the scanning system is *not smaller* than 2 m;
11. the scanned field is *at least* 25 cm x 30 cm.

The radius of *point 5* Is large, thus simplifying the construction of the SC bending magnets, because the CNAO hall is not limited in this direction.

The low ramping speed of *point 7* has been chosen to simplify the cooling of the SC magnets.

As said in Section 2, p*oint 8* is justified by the fact that the relative range variation is $\Delta R/R = 3\ \Delta p/p$ so that, for a depth R = 200 mm, with $\Delta p/p$ ±1% the range variation is ±6 mm, sufficient to follow a longitudinally moving target and equal, in total, to *six* 2-mm target slices.

4.2 The scanning system

The last three parameters of Table 5 concern the scanning system shown in Figure 11.
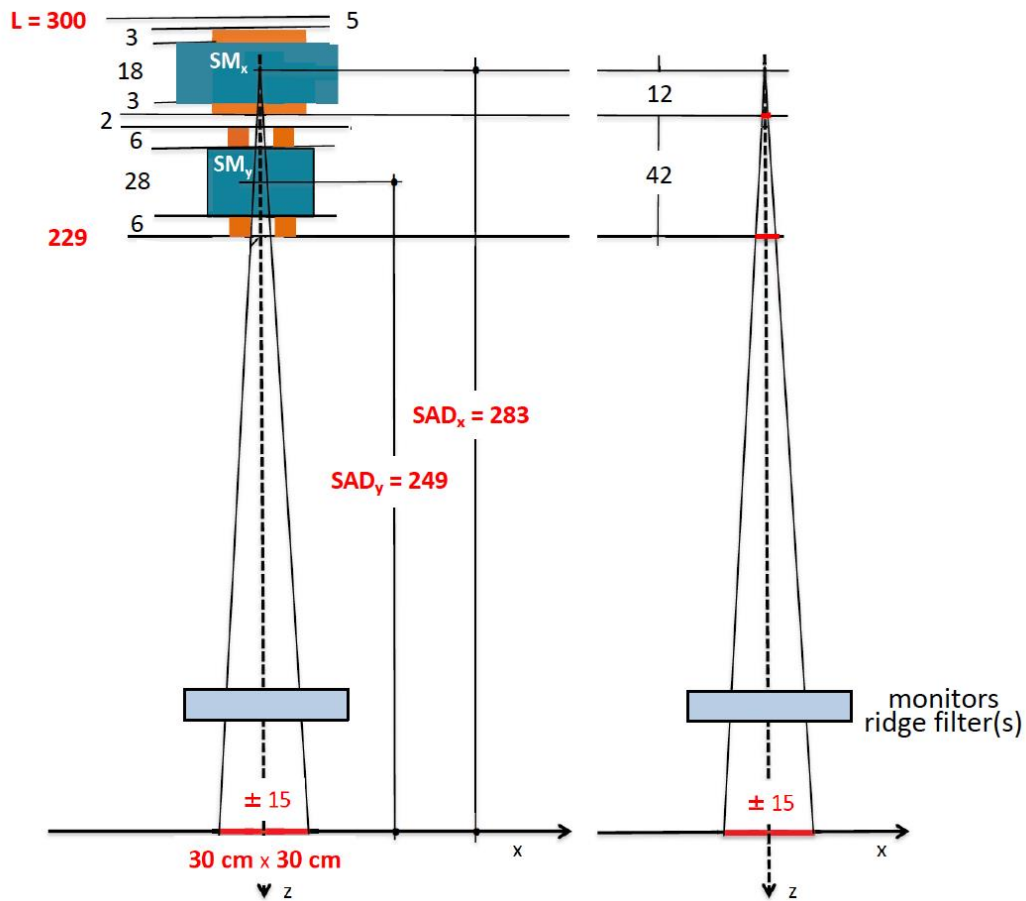

***Figure 11.** Layout of the scanning system.*

The field distributions of the two magnets, computed with Opera 3D, are shown in Figure 12.
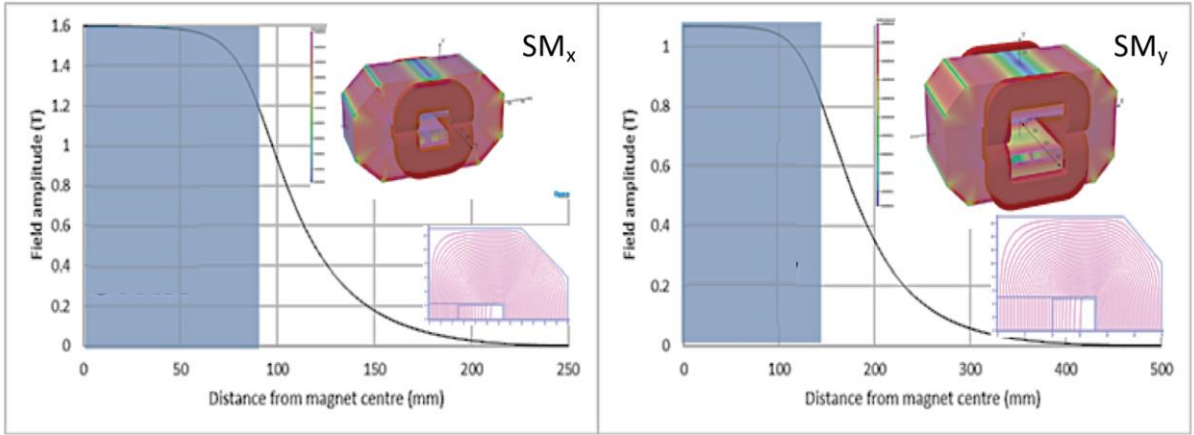
Figure 12. Magnetic field distributions of SM_x and SM_y .

The parameters of SMx and SMy are collected in Table 6, which shows that the peak fields are 1.6 T and 1.07 T respectively. To scan with the beam spot the (30 cm x 30cm) treatment area of the figure at an average speed of v_{spot} = 20 mm/ms (row 9 of Table 5), the SM_x (SM_y) currents I_x (I_y) (row 19 of Table 6) have to go from -1000A to +1000 A (-750 to +750) in 300 mm/ (20 mm/ms) = 15 ms, so that the maximum rates are

$$(\Delta I_x / \Delta t) = (\Delta I_y / \Delta t) \leqq 135\ (100)\ \text{A/ms}\quad \text{(Scanning Magnets)} \tag{11}$$

Table 6. Parameters of the two Scanning Magnets of Figure 18.

Quantity	Unit	SMx	SMy
1. Source Axis Distance SAD	cm	**283**	**249**
2. Yoke length	cm	180	280
3. Width	mm	530	650
4. Height	mm	310	400
5. Total length (with coils)	mm	**240**	**400**
6. Inter-pole gap	cm	**45**	**100**
7. Magnetic length	mm	220	370
8. Number of coils		2	2
9. Number of turns/coil		30	60
10.Peak current	A	**1000**	**750**
11.Inductance	mH	3.4	17
12.Resistance	mOhm	45	115
13.Stored energy	kJ	1.7	4.8
14.Power at max current in DC	kW	45	65
15.Peak field amplitude	T	**±1.60**	**±1.07**
16.Maximum bending angles	mrad	**±53**	**±60**

The displacements corresponding to the rates of Eq. (11) are

$$(\Delta x / \Delta I) = (\Delta y / \Delta I) = 0.25\ \text{mm/A}. \qquad \text{(Scanning Magnets)} \tag{12}$$

The quantities defining the inter-pole gaps are collected in Table 7.

Table 7. *Contributions to inter-pole gaps of the Scanning Magnets*

Quantity	Unit	SMx	SMy
1. Beam (±3 sigmas)	mm	±14	±14
2. Alignment error	mm	±1.5	±1.5
3. Beam positioning error	mm	±2.0	±2.0
4. Vacuum chamber thickness	mm	±5.0	±5.0
5. Scanning field projection ([a])	mm	0	±25.5
6. Total = 1+2+3+4+5	mm	±22.5	±48
7. Inter-pole gap	mm	**±45**	**±50**

([a]) from previous magnet, in the gap direction (see Figure 11).

4.3   Power supplies of the Scanning Magnets

The scanning magnets of Figure 11 and Table 6 require fast and powerful power supplies, which will have to be one of the main focuses of the future studies of the SIGRUM project.

Considering beam spot steps $\Delta x = \Delta y$ = 2.0 mm (row 2 of Table 5) that have to be performed in 0.10 ms (row 10 of Table 5), Eq. (12) implies current variations

$$\Delta I_x = \Delta I_y = \text{8 A   in   0.1 ms,} \tag{13}$$

as represented in Figure 13. As mentioned in Section 3.3, since some time is needed to switch the current on and off, during these short steps the current rate has to be larger than the average one indicated in Eq. 11.
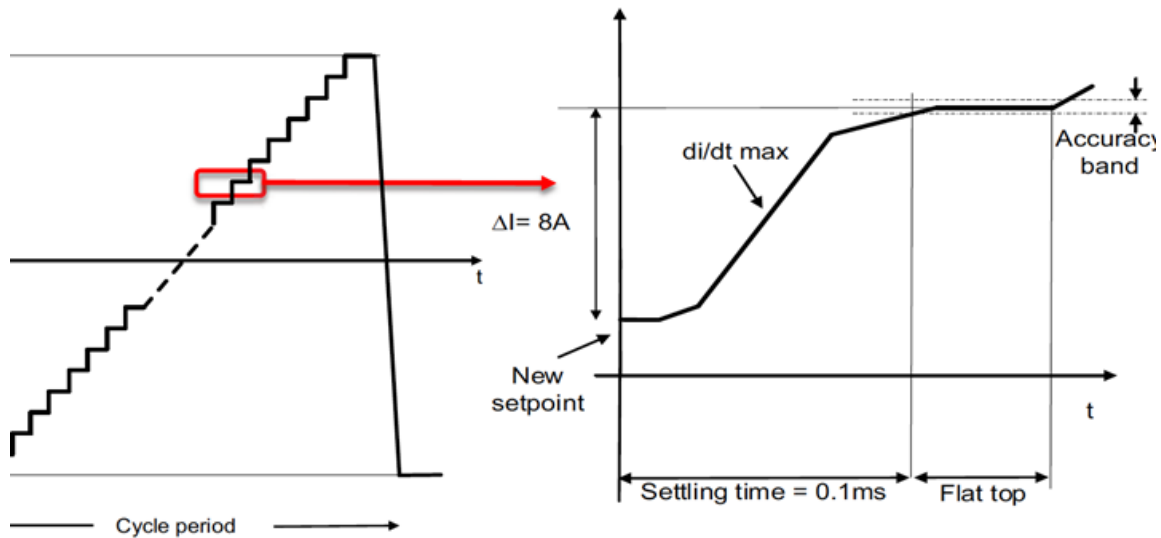

Figure 13. Steps in the currents of the Scanning Magnets.

During a treatment the current steps may be much larger, corresponding, for instance, to the large transverse displacements needed to move the beam spot from one edge of a tumour target to the other with the (average) current rate of Eq. 11.

It has to be underlined that the accuracy of the current regulation is driven by the required spot position precision, which at present has been fixed at $\pm$ 0.1 mm.

14

Several converter topologies were studied (serial, parallel, serial-parallel configuration of power modules) and the parameters of the most promising solution concerning the four quadrants converter (bipolar in current and voltage) are collected in Table 8.

Table 8. Parameters of the SMx and SMy converter, for the baseline requirements of ± 0.1 mm precision and 0.10 ms settling time

Quantity	Unit	SMx	SMy
1. Max Current I_{Max} (peak and DC)	A	±1000	±750
2. Max Voltage V_{Max}	V	±650	±1'950
3. Max Power W_{Max}	kW	±650 – 45 average	±1'460 peak – 65 average
4. Current step	A	13.33	±10
5. Current accuracy	A	±0.11 (±110 ppm of I_{Max} derived from ± 0.1mm precision)	±0.083 (±110 ppm of I_{Max} derived from ± 0.1mm precision)
6. Settling time (each current step)	ms	0.1	
7. di/dt on each current step	A/ms	191	115
8. Converter Topology	-	4 power modules in parallel (650V/250A each)	6 power modules – 2 set of 3 modules in series put in parallel (650V/375A each)
9. Switching frequency Fsw	Hz	10'000 (producing a 0.033 A peak-peak current ripple corresponding to ±0.05mm beam position excursion)	
10. Small signal current loop Bandwidth	Hz	5'000	4'000

Although the power converters seem feasible, at these power levels and high dynamics and precision, their design is challenging, and requires significant engineering efforts. Furthermore:
-   The characteristics (volume and cost) of the power converter are mainly driven by the settling time on each current step: the relaxing of this parameter would have an impact of their complexity and cost.
-   The Control requirements impose the need of a high precision and high-speed Control Electronics.

A development would require a significant resource support to develop the power modules and adequate high speed and high precision electronics to drive such modular converters, because no controller exists at CERN with these performances (and there is no possible synergy with future projects either).

In order to have a feasible solution within the same time scale of the 3T-magnet gantry and based on improved CERN existing systems, a preliminary investigation was done assuming relaxed requirements. Table 9 presents the parameters of a solution obtained by relaxing the settling time specifications (e.g. 0.20 ms) and spot precision (e.g. ± 0.3 mm).

Table 9. Parameters of the SMx and SMy converter, for the relaxed requirements of ± 0.3 mm precision and 0.20 ms settling time

Quantity	Unit	SMx	SMy
1. Max Current I_{Max} (peak and DC)	A	±1000	
2. Max Voltage V_{Max}	V	±650	±1'348
3. Max Power W_{Max}	kW	±650 – 45 average	±1'300 peak – 68 average
4. Current step	A	13.33	
5. Current accuracy (derived from stop position precision of 0.3 mm)	A	±0.33 (±333 ppm of I_{Max})	
6. Settling time (each current step)	ms	0.2	
7. di/dt on each current step	A/ms	135	
8. Converter Topology	-	4 power modules in parallel (650V/250A each)	4 power modules – 2 parallel sets, each made of 2 modules in series (650V/500A each)
9. Switching frequency Fsw	Hz	10'000 (producing a 0.167 A peak-peak current ripple corresponding to ±0.15mm beam position excursion)	
10. Small signal current loop Bandwidth	Hz	5'000	3500

This solution, with such a set of relaxed requirements, is indeed feasible with upgraded existing control electronic platforms (while the power side has to be redesigned). Iterations with the beam dose delivery experts and clinical users are required to agree on the final specifications.

4.4   Layout of the gantry

The layout of the gantry, shown in Figure 13, foresees two cold bending sections.

The first 45^0 bending is achieved with two combined function 22.5^0 dipoles and a quadrupole in between, to form an achromatic system. The second bending section is of 135^0 and it is achromatic as well, with 3 combined function dipoles of 45^0 interleaved by two quadrupoles.

The choice to have achromatic bending sections is motivated by the will to keep dispersion small and under control, resulting in a relatively large momentum acceptance. This is achieved by the superconducting quadrupole(s) between the dipoles. Moreover, a small gradient in the combined function magnets helps in providing vertical focusing, keeping both horizontal and vertical beta function small.

The 5 (warm) quadrupoles in the straight section at 45°, plus the 2 quads at the beginning, are used to fulfil the optics requirements:
- achromaticity;
- optics is independent of the gantry rotation angle;
- magnification factor of beam size (from the gantry coupling point to the isocentre) G=1;
- divergence is zero at the gantry coupling point and at the isocentre;

16

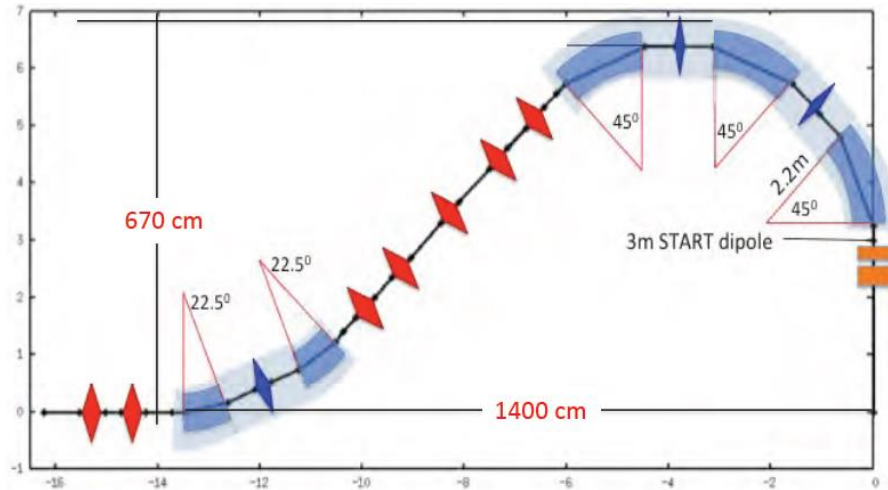- maximum beam size including the 1% momentum offset is within the +/-30 mm aperture.

Figure 14. *The gantry requires two 22.5° bending magnets (contained in the first cryostat) and three 45° bending magnets (contained in the second cryostat).*

It is worthwhile noting that the external radius of the gantry would be 5.9 m (as the one of the present NIRS gantry of Figure 1) instead than 6.7 m of Figure 14 if the bending field could be increased from 3.0 T to 3.5 T and the SADs of Figure 17 would be reduced from 283 cm to 234 cm and from 249 cm to 200 cm respectively. In this case *with the same power supplies* the treatment field would be 25 cm x 24 cm.

4.5 Optimized optics

The optics functions, from MADX computations, are shown in Figure 15.
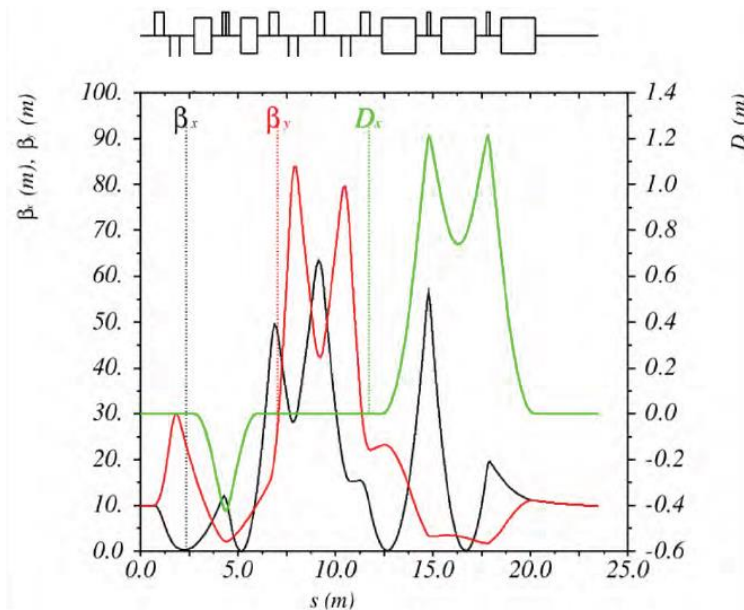
Figure 15. *Gantry optics. Initial $\beta_x = \beta_y = 10$ m, $\alpha_x = \alpha_y = 0$.*

The √5 sigmas beam widths, including the excursion due to the momentum offset, are plotted in Figure 16, where the beam size is computed with the following formula, in order to take into account the direct contribution of the dispersion:

$$S^*_{x,y}(s) = \sqrt{\beta_{x,y}(s)\varepsilon_{Tx,y}} + +D_{x,y}(s)\, dp/p, \qquad (14)$$

$\varepsilon_{Tx,y}$ is the the total geometrical emittance calculated as five times the root-mean-square (RMS) emittance ($\varepsilon_{Tx,y} = 5\,\varepsilon_{rms\,x,y}$) and $\Delta p/p = \pm1\%$ is the maximum momentum offset[12] .
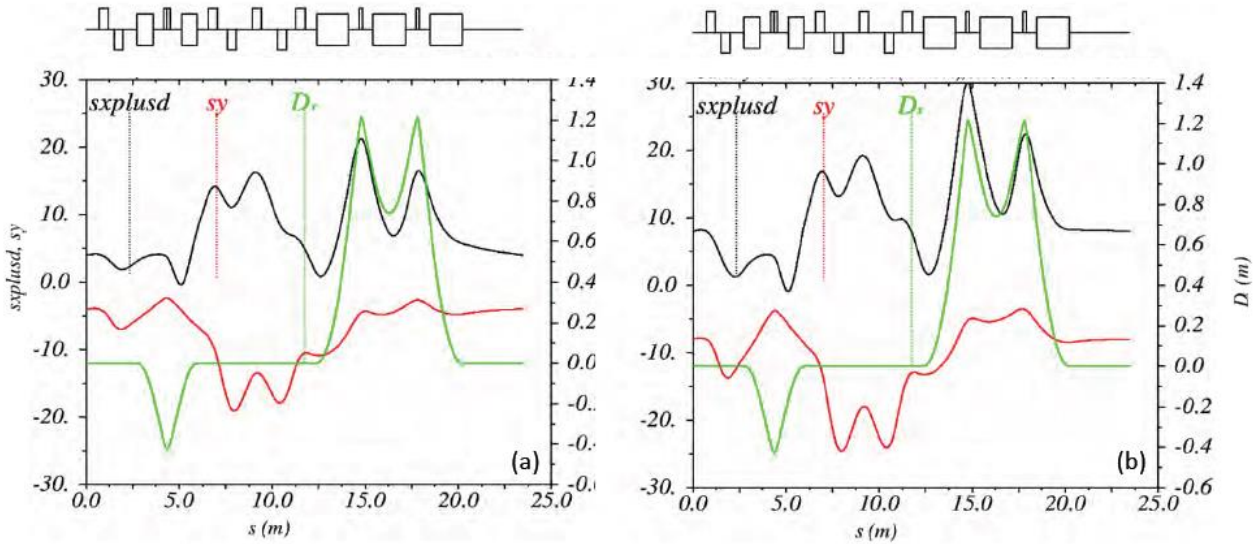

Figure 16. *Horizontal and vertical beam sizes with offset due to momentum excursion, for the two cases mostly used in operation. Left: spot size of 4mm at the isocentre @ 430 MeV/u. Right: spot size of 8 mm @ 100 MeV/u. In both cases the momentum acceptance is 1%.*

It has to be remarked that detailed tracking with error studies have not yet been performed.

The beam optics has been optimized for FWHM transverse dimensions of the spot in the range 4.0 mm – 8.0 mm with a momentum acceptance of 1%. A spot size of 10 mm can also be achieved and in this case the momentum acceptance is still 0.6%[13].

5. Mechanical structure of the gantry

The choices that drive the design of the gantry mechanics have been discussed in Section 2:
   a) avoid accessories that are not absolutely needed for the gantry rotation:
   b) no counterweight;
   c) use of the cryostats as structural elements to increase the support rigidity;
   d) rotation, in the angular range +110° and -110°, by an electric motor with planetary gear, as shown in Figure 5;
   e) attachment to the wall of the treatment room.

These simplifications lead automatically to a light gantry that can be transported from the construction company to the treatment site as a single piece and can be mounted in few days.

Results of a Finite Element Analysis on the 4 T gantry are represented in Figure 17. The 3 T gantry of Figure 14 is lighter but has a larger diameter, so that the results will be very similar.

---

[12] The values have been taken from the PIMMS study of Ref 8.
[13] This is sufficient to vary the longitudinal position of the Bragg peak of +/-4.2mm at a 200 mm depth (water equivalent), corresponding to more about 3 longitudinal planes, without changing the field in the superconducting magnets.
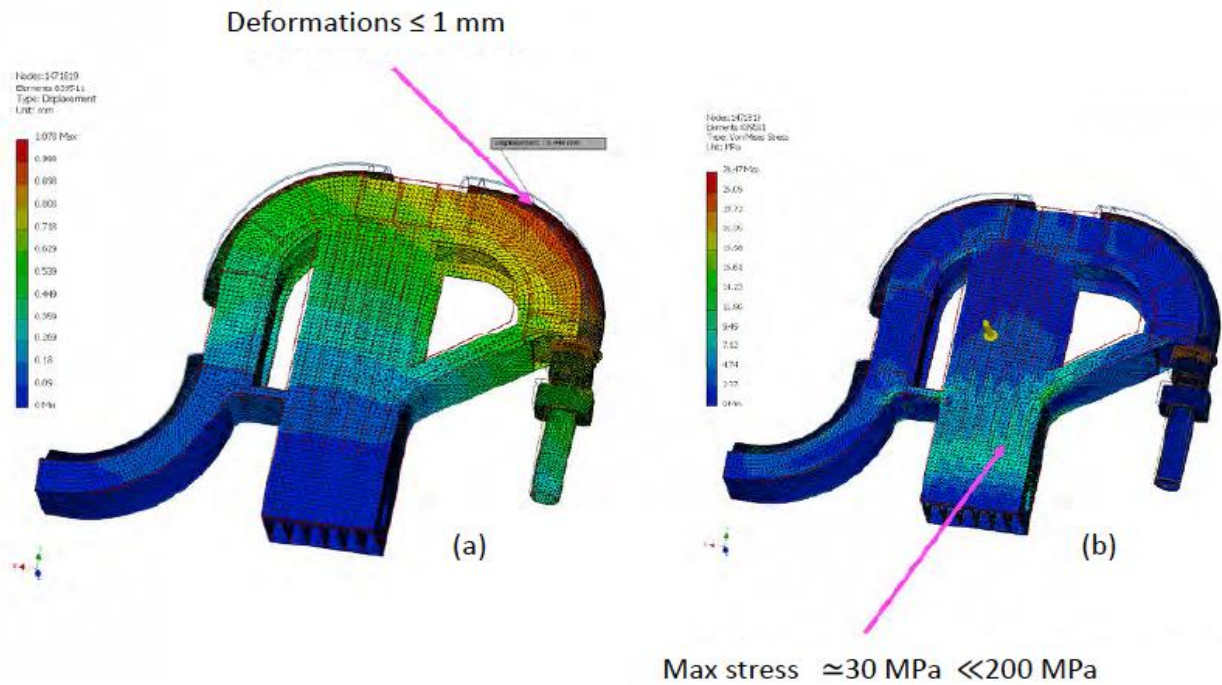
Deformations ≤ 1 mm

Max stress ≃30 MPa ≪200 MPa

Figure 17. *The welded-plate support of the gantry of Figure 6 has been optimized with many Finite Elements studies. This figure present a scheme that correspond to distortions of less than 1 mm.*

In the future study different gantry mechanical structures, based on the same principles, will be compared: from the continuous elements integrating the magnets to increase the rigidity, as in Figures 6b and 17, to the reticular-structure example shown in Figure 18.
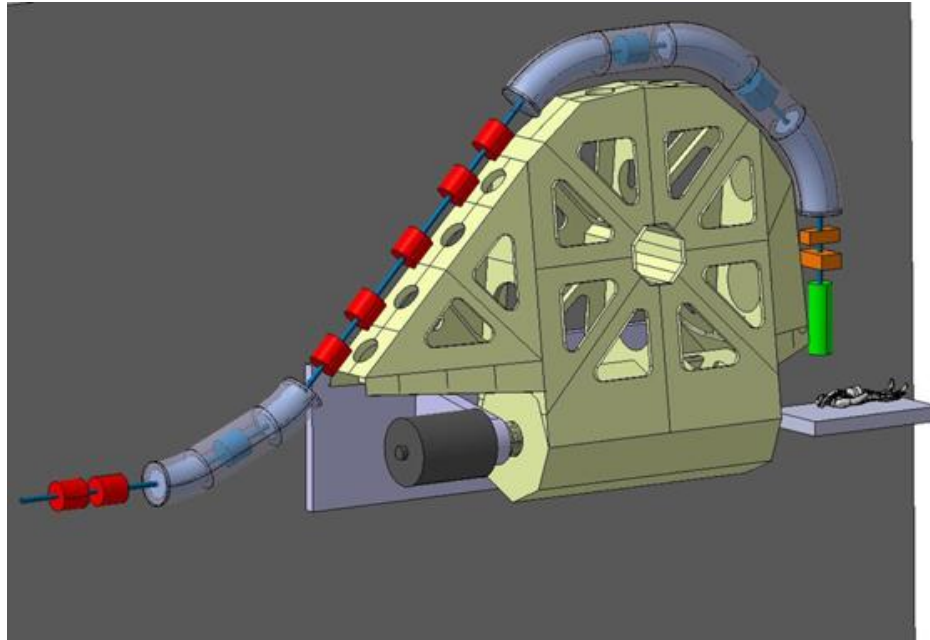
Figure 18. *One of the options for the gantry structure. Bending magnets (cold) in grey, quadrupoles in red (warm) and blue (cold), scanning magnets in orange, nozzle & dosimetry section in green. (Courtesy of L. Gentini)*

6. A demonstrator for the superconducting combined function magnets

Development of conduction cooled curved superconducting magnets have clear potential for compact hadron therapy gantries and may also be considered, with certain additional features (faster ramping), for compact medical synchrotrons where a cryogenic system based on liquid helium bath is not an option.

A combined function superconducting bending magnet design based on collared cos-theta coils is proposed for SIGRUM. These magnets, based on the technologies extensively developed for the LHC project, include several gantry-specific features that shall be developed and validated by a demonstrator magnet. The main development areas include fabrication of epoxy-impregnated cos-theta coils with 2.2 m radius of curvature along with the assembly of the surrounding curved cold mass. The demonstrator magnet test will also serve to validate and fine-tune the advanced numerical models for the electromagnetic and thermal optimisation of the final gantry magnet.

The present gantry design includes two 22.5° magnets in the first cryo-assembly and the final bending section is composed of three 45° magnets in common cryostat. To make a maximum use of the existing infrastructure, notably the collaring and yoking presses, the final choice of the demonstrator magnet length will be made after a more detailed study of the assembly tooling. The 45° magnet would address all manufacturing challenges of the final magnets. However, the lateral space requirement due to the sagitta may be a limiting factor.

6.1 Electromagnetic design

Two alternative designs have been studied, a high-current and low-current version with nominal currents of 2144 A and 584 A, respectively.

High-current design

The main parameters of the high current version of the combined function bending magnet demonstrator are given in Table 9.

Table 9. Main parameters of the high current version

Parameter	Value	Unit
Nb-Ti strand diameter	0.48	mm
Filament diameter	6	μm
Cu:Sc ratio	1.75	
No. of strands	34	
Cable width	8.7	mm
Core thickness (stainless steel)	25	μm
B_{nom} (70-430 MeV/u)	1.11 - 3.0	T
G_{nom} (430 MeV/u)	3.5	T/m
I_{nom}	796 – 2144	A
dB/dt	0.10	T/s
Margin at 4.7/6 K	45% / 27%	
Aperture	70	mm
Yoke ID/OD	~130 / 320	mm

Bending angle	22.5°	30°	45°	
Magnetic length	0.87	1.16	1.74	m
Stored energy	23	31	46	kJ
Self inductance	6.7	13.4	26.8	mH
Coil length	1.0	1.3	1.88	m
Total length	1.15	1.45	2.05	m
Approx. mass	560	710	1020	kg
Coil sagitta (R2.207 m)	25.7	42.3	86.5	mm

The design field gradient of 3.5 T/m is generated by left-right asymmetry and the turns are arranged in four and three winding blocks on the inner and outer layer, respectively. To ensure reliable operation in the gantry, the coil was designed with a margin of 27% on the load-line at 6K.

The 8.7-mm-wide Rutherford cable considered for this design, composed of 34 ⌀0.45 mm Nb-Ti strands with 6 μm filaments, is almost identical to that used for LHC MQY outer layer coil and features a 25-μm-thick stainless-steel core to minimize the transient losses during the operation. Depending on a final assessment of cryogenic losses, the use of a conductor with smaller filaments may be considered for the gantry magnets at a later stage. The braided glass insulation for epoxy impregnation is similar to the cable insulation of the HL-LHC MQXF.

The magnet cross-section, shown in Figure 19, was first optimized in 2D to meet the specified higher field harmonics of below 10^{-3} level at a radius of 20 mm. The transfer function of the main field components (dipole and quadrupole) are only slightly non-linear towards the nominal field of 3 T due to the iron saturation. This will be further optimized in parallel with the structural design optimization of the collars.
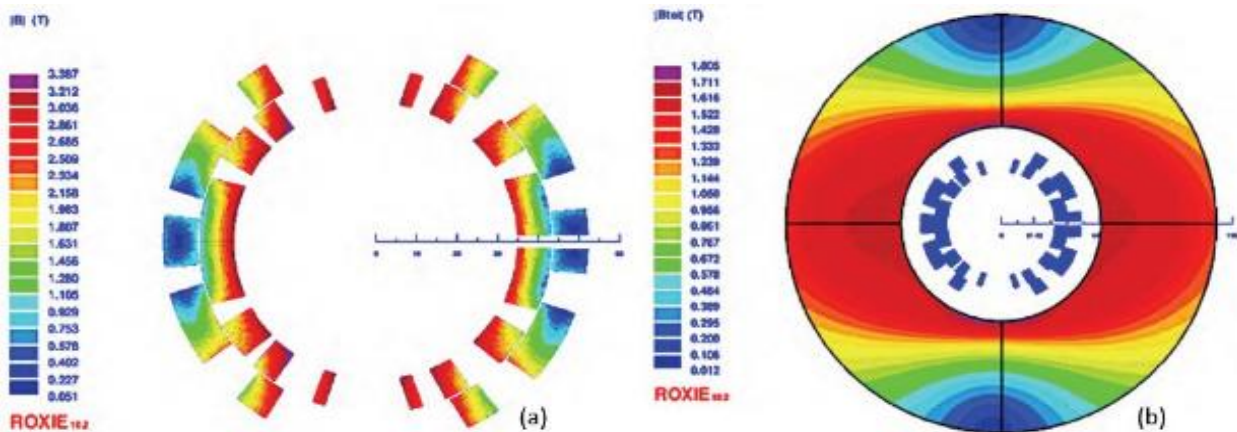

Figure 19. *Cross-section of high-current design: coils (left) and yoke (right).*

For the 3D-analysis the return end of the coil was modelled in ROXIE[14]. The relative position of the winding blocks at the ends were not optimized for the integrated field quality, nor the minimum peak field, as these will be addressed at a later stage for the detailed engineering design. The straight 3D coil geometry was exported from ROXIE to Opera-3D and, by coordinate transformation, to a curved geometry with the radius of curvature of 2.207 m.

---

[14] ROXIE, https://espace.cern.ch/roxie

Table 10 lists the integrated field components of a 30° magnet calculated from line integrals along a 40° toroidal sector.

Table 10. *Integrated field quality at R20 mm of 30° magnet calculated from line integrals along 40° toroidal sector in Opera-3D.*

Parameter	Value
B1 (Tm)	3.46
G (T/m)	3.53
$B3/B1 \times 10^4$	1.9
$B4/B1 \times 10^4$	2.5
$B5/B1 \times 10^4$	3.5
$B6/B1 \times 10^4$	2.6
$B7/B1 \times 10^4$	1.6
$B8/B1 \times 10^4$	5.1
$B9/B1 \times 10^4$	2.1
$B10/B1 \times 10^4$	-0.3
$B11/B1 \times 10^4$	-0.1
Magnetic length (m)	1.155

Figure 20 illustrates the Opera-3D model that was used to analyze the effect of curved configuration and for preliminary tracking studies of the 430 GeV/u Carbon ions.
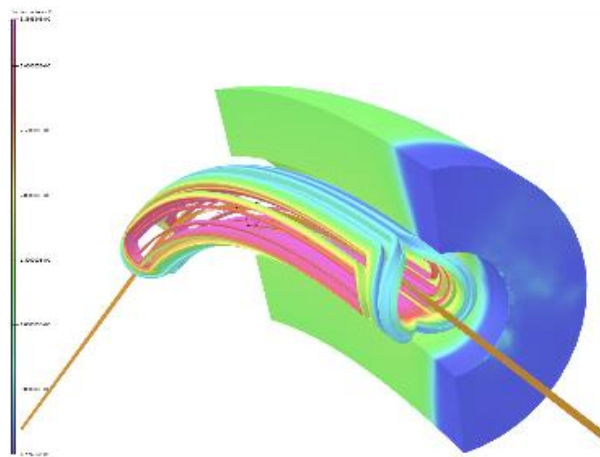
Figure 20. *Opera-3D model of the 30 ° magnet and tracking with 430 MeV/u $^{12}C^{6+}$-beam.*

Low-current design

Current leads are expected to represent a significant fraction of the cryogenic load for the superconducting magnet system of the gantry. To reduce these losses a low-current version of the combined function bending magnets was designed with a nominal current of 584 A for the 3 T bending field.

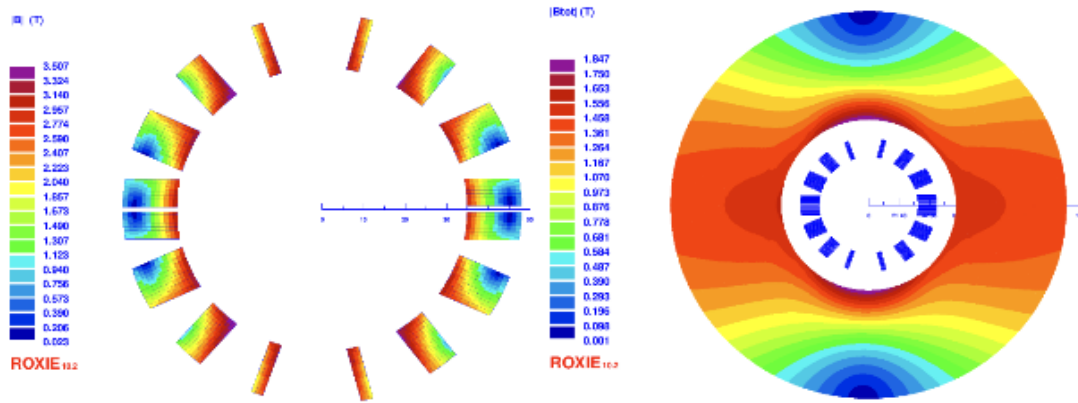The Opera-3D model of the low-current version is shown in Figure 21.

Figure 21. *Cross-section of low-current design: coils (left) and yoke (right).*

The main parameters of the low-current design are listed in Table 11.

Table 11. *Main parameters of the low-current version*

Parameter	Value			Unit
Nb-Ti wire dimensions (metal)	1.53 x 0.85			mm
Filament diameter	6			µm
Cu:Sc ratio	1.71			
PVA insulation thickness	60			µm
No of wires in cable	8			
B_{nom} (70-430 MeV/u)	1.11 - 3.0			T
G_{nom} (430 MeV/u)	2			T/m
I_{nom}	215 – 584			A
dB/dt	0.10			T/s
Margin at 4.7/6 K	37% / 18%			
Aperture	70			mm
Yoke ID/OD	~124 / 320			mm
Bending angle	**22.5°**	**30°**	**45°**	
Magnetic length	0.87	1.16	1.74	m
Stored energy	23	28	46	kJ
Self inductance	6.7	167	26.8	mH
Coil length	1.0	1.3	1.88	m
Total length	1.15	1.45	2.05	m
Approx. mass	560	710	1020	kg
Coil sagitta (R2.207 m)	25.7	42.3	86.5	mm

The single-layer coils are wound with eight rectangular PVA-insulated superconducting wires pre-assembled as a flat cable. The cable is identical to that used for combined H/V-corrector dipoles in the inner triplets of the LHC. The individual wires of the cable are connected in series on the magnet end plate. Coil fabrication with such ribbon cable is significantly more

23

challenging than with Rutherford-type cable, as even a slight hard-way strain on the cable causes the wires to split. The optimization of end spacer geometry also typically requires more iterations to minimize the voids and the mechanical strain in the cable. The electromagnetic cross-section of the magnet illustrated in Figure 21 was optimized for a nominal gradient of 2 T/m at full field according to the updated gantry specification and all higher field harmonics to 10^{-4} level.

The integrated field harmonics calculated at 20 mm radius from line integrals along a toroidal sector of 40° are listed in Table 12. The magnetic length is 1.154 m.

Table 12. *Integrated field quality at R20 mm of 30° magnet.*

Parameter	Value
B1 (Tm)	3.45
G (T/m)	2.01
B3/B1 x 10^4	-11.5
B4/B1 x 10^4	0.3
B5/B1 x 10^4	6.7
B6/B1 x 10^4	0.8
B7/B1 x 10^4	0.3
B8/B1 x 10^4	0.5
B9/B1 x 10^4	-0.8
B10/B1 x 10^4	-0.3
B11/B1 x 10^4	0.0
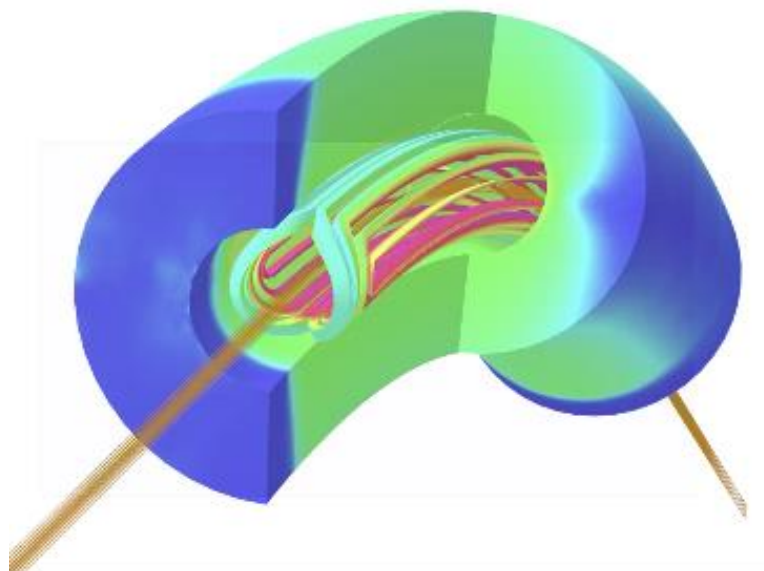
Figure 22. *Opera-3D model of the 30 ° magnet and tracking with 430 MeV/u $^{12}C^{6+}$-beam.*

6.2   Mechanical concept

The mechanical concept of the high current MBCFD1 is illustrated in Figure 23. The structure of the low-current would be very similar, except for the single-layer coil wound with the 8-way ribbon.
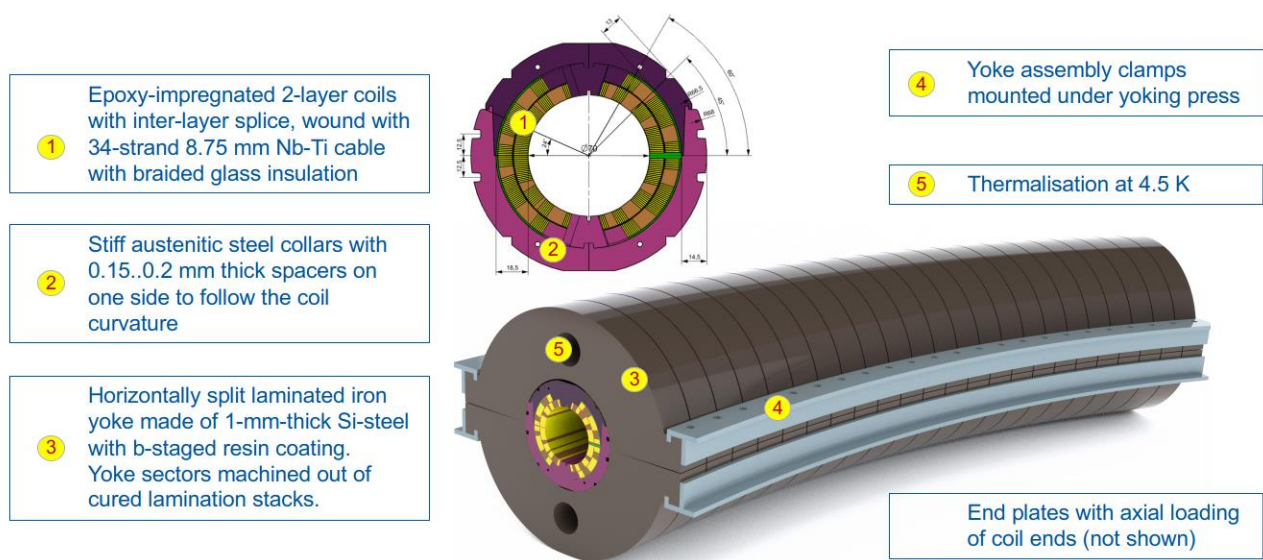
***Figure 23**. High-current demonstrator magnet mechanical concept.*

Thanks to the relatively low peak field and current density when using a collared structure, the required pre-stress is only about 50 MPa at the operating temperature. This is provided to the 2-layer epoxy-impregnated coils by stiff stainless-steel collars. The 2-mm-thick collars are pre-assembled as packs of some 50 mm and closed by trapezoidal keys under a collaring press. By adding an additional spacer of about 0.15 mm between the collars on one side of each collar pack, the collars follow the curvature of the coils. With the coil sagitta of 42.3 mm the collaring can be done under a straight collaring press utilising curved contact tooling.

The horizontally split laminated iron yoke is made of 1-mm-thick Si-steel with b-staged resin coating. Shaping the yoke can be achieved in several manners, for example by composed blocks glued and thereafter machined to their final curved shape.

The yoke halves are mounted around the collared coil with a slight radial interference to provide additional rigidity and to ensure a good thermal contact during the operation. The axial compression to the coil ends can be provided by end plates and bolts as for the LHC dipoles. The yoke halves are assembled around the collared coil under the yoking press and held together with bolted flanges at the mid-plane.

6.3   Structural analysis

The electro-magnetic Boundary Element analysis was performed in PITHIA[15]-EM to compute the Lorentz forces which were used as input in the structural model. The 2.5D structural Finite Element Analysis was performed in environment of SIEMENS Simcenter 3D[16].

The results of the structural analysis with the optimized assembly parameters show that the maximum coil stress during assembly and after cooldown, respectively 108 MPa and 81 MPa, remain well within a safe range, still ensuring that the coils are not unloaded at the maximum operational field (Figure 24).

---

[15] PITHIA Boundary Element Software: https://feacomp.com/pithia/

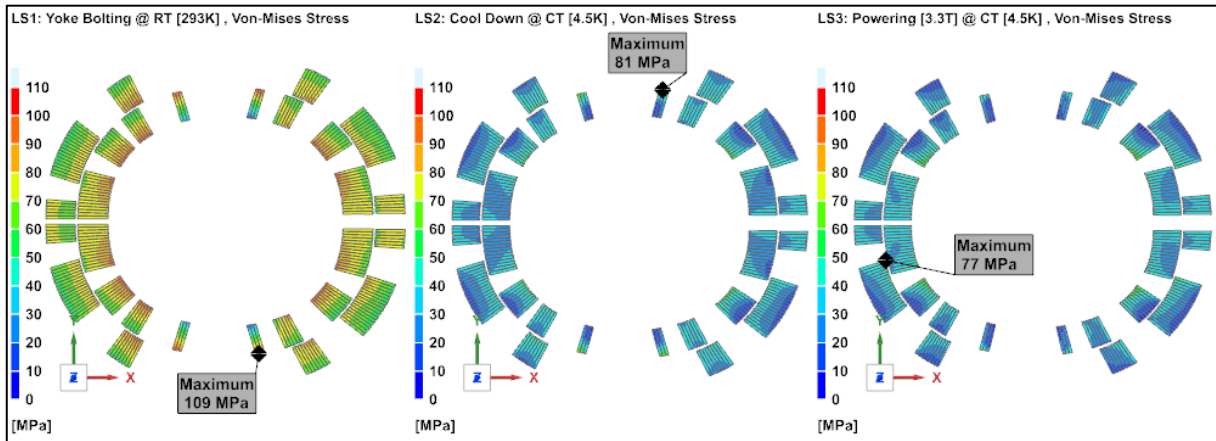[16] SIEMENS Simcenter 3D: link

Figure 24. Von Mises stress at all Load steps

Furthermore, the design ensures an extended contacting surface at the yoke - collar interface during operation of the magnet (Figure 25), which is a very important factor for the heat transfer from the coils to the surrounding structure;
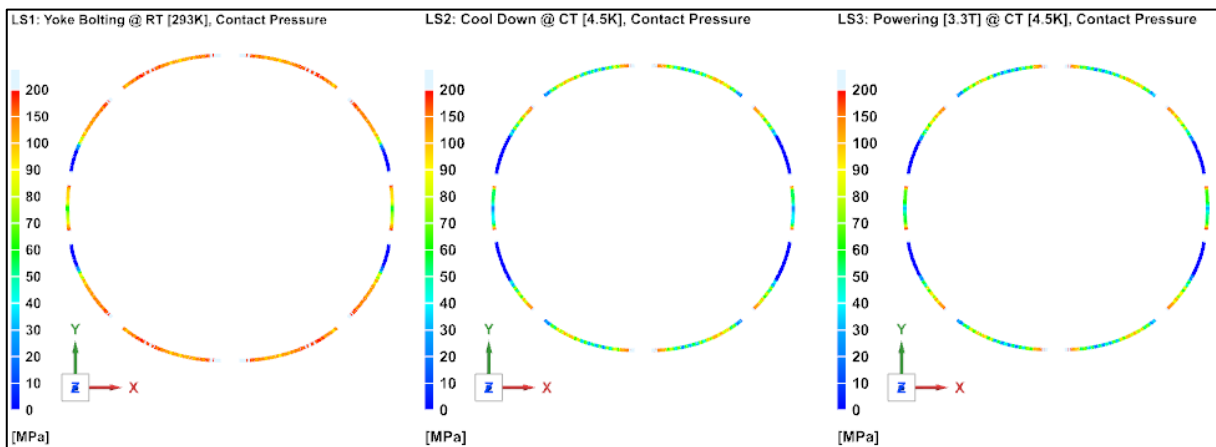

Figure 25. Contact pressure at the collar-yoke interface at all Load steps

A sensitivity analysis was also performed, showing that the magnet can be constructed with realistic manufacturing tolerances while maintaining the characteristics described above.

6.4   Transient loss analysis

During the hadron therapy cycles the magnets are continuously ramped in the field range of 1.1 T to 3 T at up to 0.10 T/s. An advanced COMSOL multiphysics 2D FE-model of the high-current design was created using the STEAM-SIGMA [17] [18] environment to study the transient losses. It includes the characteristics of the coils and the temperature and field dependence of the thermal and electrical properties of the materials in the magnet cross-section.

The two holes in the iron yoke were defined as perfect thermal sinks at 4.5 K. The inter-filament coupling losses (IFCL), inter-strand coupling losses (ISCL), and the eddy current losses (ECL) in the Cu-wedges were calculated in Comsol, whereas the persistent current losses (PCL) were computed with ROXIE and imported to the Comsol model as uniformly distributed loss

---

[17] L. Bortot, B. Auchmann, I. Cortes Garcia, A. M. Fernandez Navarro, M. Maciejewski, M. Prioli, S. Schöps, A. Verweij, *A 2-D Finite-Element Model for Electro-Thermal Transients in Accelerator Magnets*, IEEE Transactions on Magnetics, 2017.

[18] STEAM: *Simulation of Transient Effects in Accelerator Magnets*, https://espace.cern.ch/steam/.

of 201 W/m^3. The majority of the transient losses in the superconducting coils occurs at low fields and a conservative approach of current ramping between 0 and 2144 A was chosen for this analysis. Figure 26 shows the temperature distribution and the heat flux after ramping the magnet for 130 seconds at 0.10 T/s. The resulting temperature rise is 190 mK.
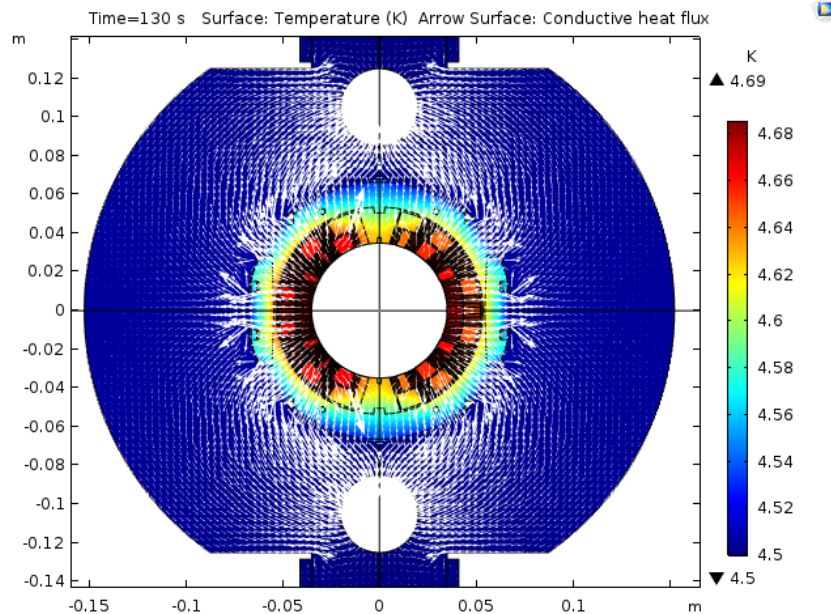

Figure 26. *Temperature distribution and heat flux of the reference case after 130 s.*

In addition to the reference case, two "worst case" scenarios with pessimistic assumptions were analysed and summarised over the powering cycle of 60 s in Table 13.

Table 13. *Summary of transient analysis of reference and the two "worst case" scenarios.*

Quantity	Unit	Reference case	Worst Cu-wedges	Worst G10-wedges
Ramp rate, dB/dt	T/s	0.1	0.1	0.1
Powering cycle	s	60	60	60
Strand transverse resistivity factor, fRho$_{eff}$		1	1/3	1/3
Persistent Current Loss per cycle, PCL	J/m	26.39	105.58	105.58
Inter-Filament Coupling Loss per cycle, IFCL	J/m	8.52	25.56	25.56
Inter-Strand Coupling Loss per cycle, ISCL	J/m	0.46	0.46	0.46
Eddy current loss in wedges per cycle, ECL	J/m	8.98	8.98	0.00
Losses in collar and iron yoke per cycle	J/m	30.34	30.34	30.34
Total losses in the magnet, per cycle	J/m	74.69	170.92	161.94
Total transient mean loss during a cycle	W/m	1.24	2.85	2.70
Temperature rise	mK	190	700	800

In the "worst case" models, conservative assumptions were selected, namely the PCL was multiplied by four, strand transverse resistivity (fRHO$_{eff}$) divided by three, ground insulation thermal conductivity divided by four, and two times higher thermal resistance was chosen for the collar-yoke interface.

In order to evaluate the effect of repetitive power cycling, steady-state simulations are performed, where the average powers PCL, IFCL, ISCL, and ECL were assigned uniformly in the coil. Figure 27 shows the temperature distribution and the heat flux in the magnet cross-section for the "worst case" scenario, with wedges made of copper or of epoxy-glass.
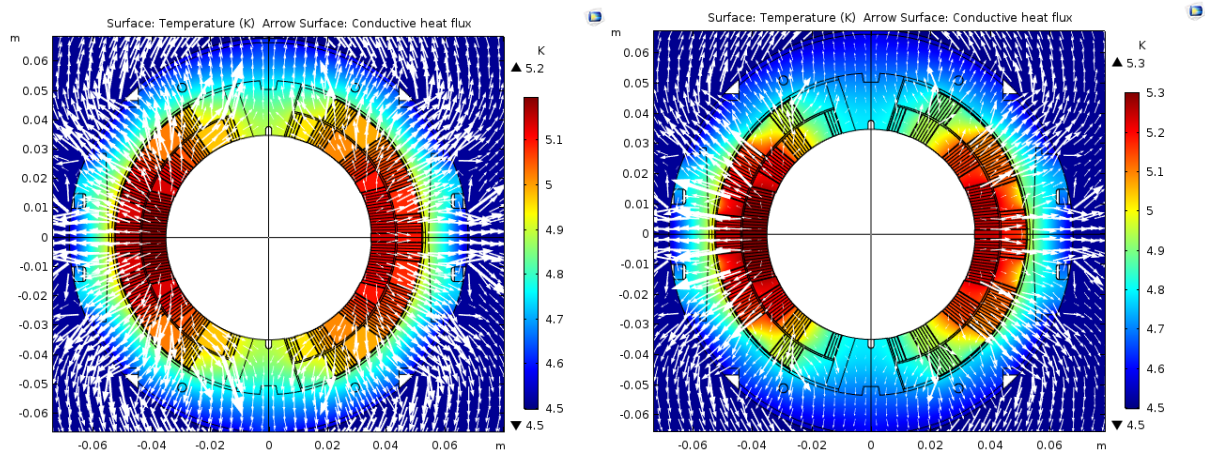

Figure 27. *Temperature distribution and heat flux for the "worst case" scenarios with Cu-wedges (left) and epoxy-glass wedges (right).*

The results indicate that, despite the presence of eddy current losses in the Cu-wedges, their higher thermal conductivity helps spreading the heat across the coil parts resulting in somewhat lower peak temperature. The temperature increase after the steady-state condition is reached are 700 mK and 800 mK with copper and epoxy-glass (G10) wedges, respectively. At the nominal current the current-sharing temperature is about 6 K, i.e. 1.5 K above the operating temperature.

In addition to the transient losses arising from the coils, the eddy current and hysteresis losses from the iron yoke along with eddy current losses in the collars, keys etc shall be accounted for the total cryogenic load of the magnet. A preliminary estimate of 0.88 W can be obtained by scaling the results of the Discorap[19] magnet developed by INFN. Therefore, a total dynamic loss in the range of 2.2 W to 5.0 W is expected to be extracted from the 45° bending magnet by the cryogenic system of the gantry, considering the reference and "worst case" scenarios, respectively.

The low-current design transient coil losses are expected to be somewhat lower and the heat conduction somewhat more efficient than the high-current version. Table 14 compares in a qualitive way the transient coil losses from ROXIE models over two powering cycles.

Table 14. *Transient coil losses for low- and high-current design over 120 s cycle.*

Loss source	Unit	Low-current design	High-current design
PCL	J/m	26.9	32.4
IFCL	J/m	12.3	10.6
ISCL	J/m	n/a	0.61
Total	J/m	39.2	43.8

---

[19] *INFN-13-06/GE 22 th May 2013, Technical Design Report of the Superconducting Dipole for FAIR SIS300.*

6.5 Quench protection

The baseline quench protection system for the high-current design relies on an energy-extraction system with resistance R_{EE} connected in series with three magnets of 1.74 m magnetic length. The quench protection analysis was performed with the STEAM-LEDET program[20], which relies on a 2D electro-thermal model of the magnet including inter-filament and inter-strand coupling losses, thermal diffusion between turns, and a simplified electrical circuit. In the present analysis, inter-strand coupling loss is neglected due to the presence of core in the cable. The hot-spot temperature is calculated under conservative assumptions, namely in adiabatic conditions (heat generated in the hot-spot is not diffused longitudinally, nor transversally), assuming the highest magnetic field in the coil cross-section, and neglecting the resistance developed in the hot-spot (only including coil resistance resulting from the quench-back).

High-current design

In the analysis, it is assumed that the times to detect the quench, validate the detection, and open the energy-extraction switch are 5 ms, 10 ms, and 5 ms, respectively. The value of R_{EE} is selected as a compromise between reducing the hot-spot temperature, calling for higher R_{EE}, and reducing the peak voltage to ground, calling for lower R_{EE}.

Figure 28 shows the simulated adiabatic hot-spot temperature versus peak voltage to ground, after a quench at nominal current, obtained by considering varying R_{EE} in the range between 15 and 150 mΩ. Two sets of simulations are presented: including inter-filament and inter-strand coupling losses, which is more realistic, and neglecting them, which is more conservative. The difference between the two cases is negligible.
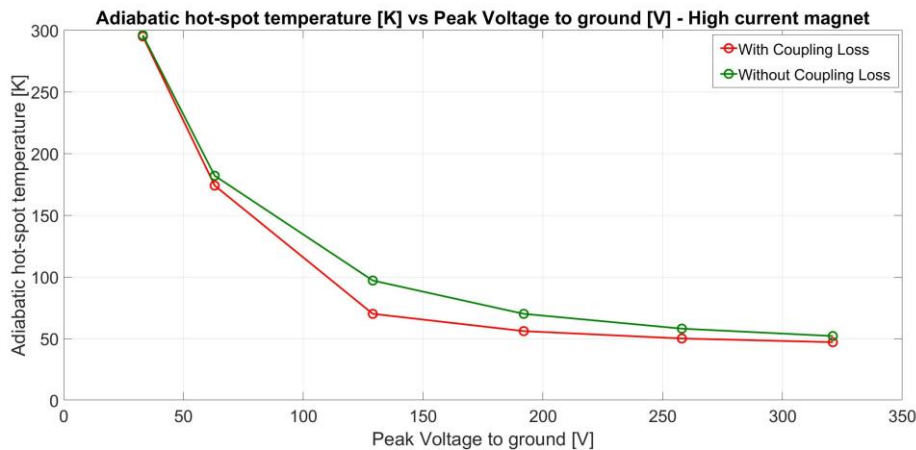

Figure 28. *Simulated adiabatic hot-spot temperature versus peak voltage to ground, after a quench at nominal current, obtained by considering varying R_{EE} in the range between 15 and 150 mΩ. High-current magnet design.*

The selected value of R_{EE} is 90 mΩ, which results in a hot-spot temperature below 60 K (without including coupling loss: below 75 K) and a peak voltage to ground below 130 V. This design relies very little on quench-back to protect the magnets.

---

[20] E. Ravaioli, B. Auchmann, M. Maciejewski, H. ten Kate, and A. Verweij, *Lumped-element dynamic electro-thermal model of a superconducting magnet. Cryogenics*, 2016. [Online]. Available: http://www.sciencedirect.com/science/article/pii/S0011227516300832.

The simulated magnet current during the transient and 2D temperature distribution in the coils of the magnet where the quench started are shown in Figures 29 and 30, respectively. All coil turns are transferred to the normal state due to quench-back between 60 and 400 ms after the energy-extraction system is triggered. The energy extracted by the energy-extraction system is about 69% of the energy stored in the three magnets, and the remaining 31% is deposited in the coil windings.
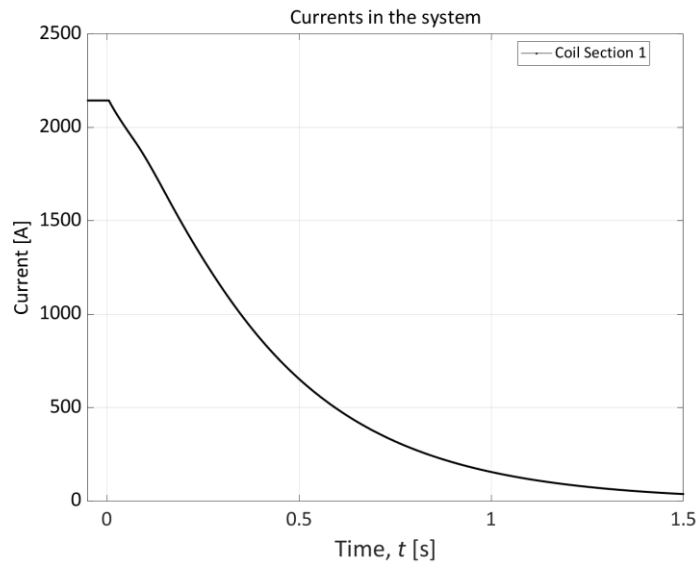

Figure 29. *Simulated magnet current after a quench at nominal current. Three magnets in series protected by a 90 mΩ energy-extraction system triggered at t=5 ms..*
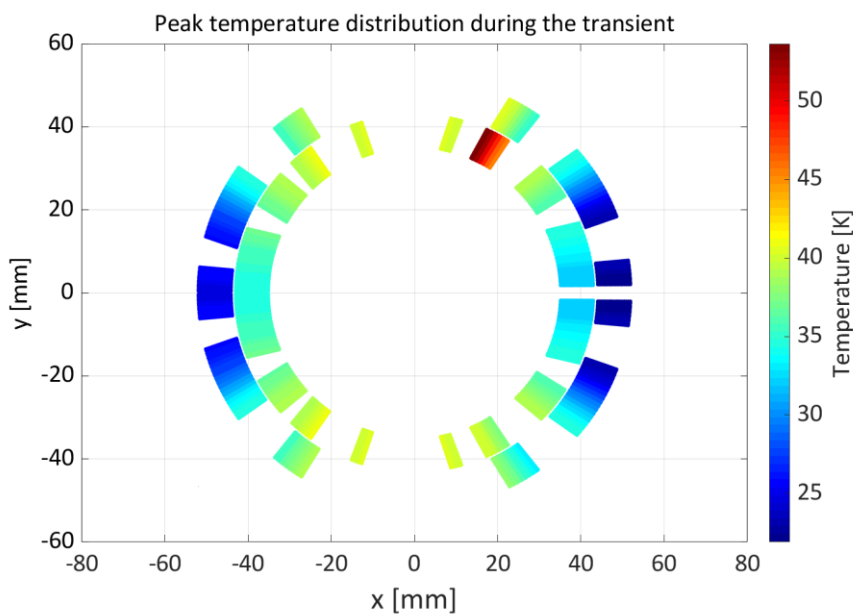
Figure 30. *Simulated 2D temperature distribution in the coil turns after a quench at nominal current. Three magnets in series protected by a 90 mΩ energy-extraction system triggered at t=5 ms.*

Low-current design

Similar simulations have been performed for the low-current magnet design. In the analysis, it is assumed that the times to detect the quench, validate the detection, and open the energy-extraction switch are 240 ms, 10 ms, and 5 ms, respectively.

Figure 31 shows the simulated adiabatic hot-spot temperature versus peak voltage to ground, after a quench at nominal current, obtained by considering varying R_{EE} in the range between 0.6 and 3 Ω. The difference between the simulations including inter-filament coupling loss, or not, is very significant, especially for low values of R_{EE}. Even if the case including coupling loss is more realistic, a prudent approach is followed, which aims at maintaining the hot-spot temperature below 350 K even without coupling loss. This eliminates the risks of relying on quench-back for the protection, a phenomenon that depends on not very well known conductor parameters (chiefly the effective transverse resistivity).
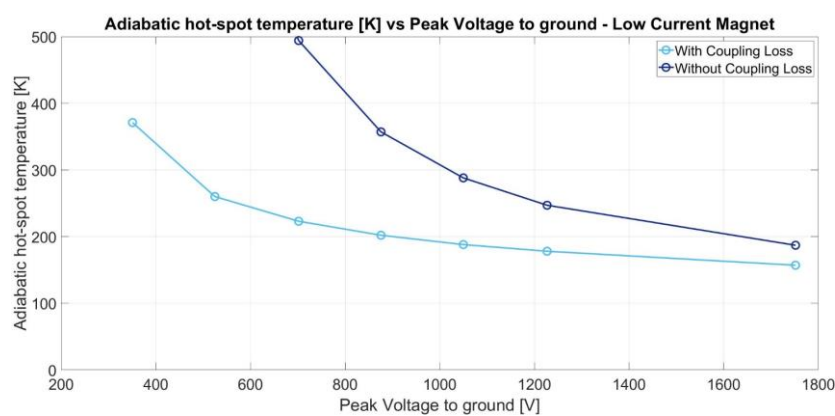

Figure 31. *Simulated adiabatic hot-spot temperature versus peak voltage to ground, after a quench at nominal current, obtained by considering varying R_{EE} in the range between 0.6 and 3 Ω.*

The selected value of R_{EE} is 1.65 Ω, which results in a hot-spot temperature below 200 K (without including coupling loss: below 320 K) and a peak voltage to ground of below 1000 V.

The simulated magnet current during the transient and 2D temperature distribution in the coils of the magnet where the quench started are shown in Figures 32 and 33, respectively.
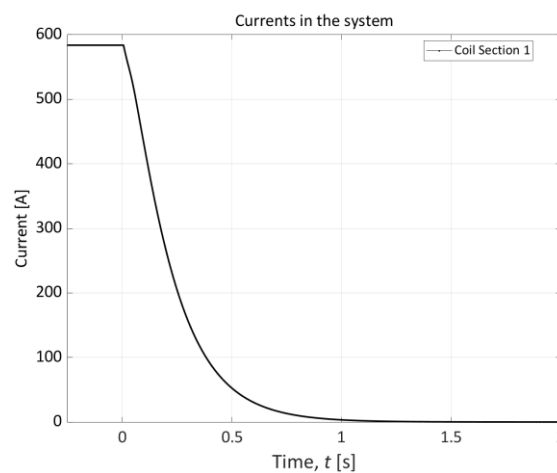

Figure 32. *Simulated magnet current after a quench at nominal current. Three magnets in series protected by a 1.65 Ω energy-extraction system triggered at t=5 ms.*
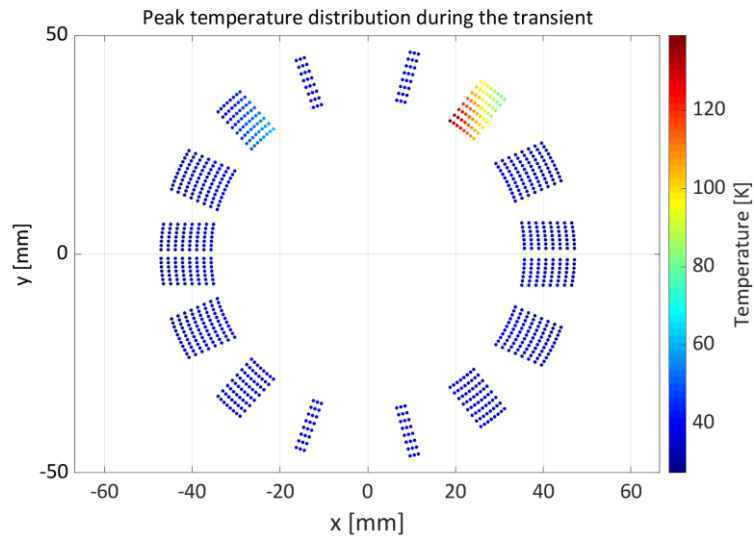
Figure 33. *Simulated 2D temperature distribution in the coil turns after a quench at nominal current. Three magnets in series protected by a 1.65 Ω energy-extraction system triggered at t=5 ms. Low-current magnet design.*

All coil turns are transferred to the normal state due to quench-back between 30 and 140 ms, after the energy-extraction system is triggered. The energy extracted by the energy-extraction system is about 58% of the energy stored in the three magnets, and the remaining 42% is deposited in the coil windings.

7. Summary and outlook

In summary, the conceptual design presented in this paper has shown that the carbon ion gantry of Figure 14 (p. 16) can be built with the techniques available today. The next steps for completing a Technical Design Report, and then initiating the construction phase are:

(i) the construction of a 45° 3-tesla bending magnet (Figures 22 and 23), which is feasible in a couple of years with the experience that CERN has in the realization of SC cosine-theta magnets,

(ii) the detailed design of the two Scanning Magnets (Figure 12) and their power supplies that, as discussed in Section 4.3, are challenging devices of this system.

From the work done it can also be concluded that, with a 3.5 T bending field - rather than 3.0 T - and SADs equal to 249 cm and 200 cm - rather than 283 cm and 234 cm as in Figure 11 - the external diameter of the gantry would be 5.9 m instead than the 6.7 m indicated in Figure 14.

With the power supplies described in Section 4.3, the scanned field would be 25 cm x 24 cm, but the 30 cm x 30 cm field could be recuperated with more powerful power supplies and/or by relaxing some of the specifications, in particular the requirement that a 2 mm transverse step of the beam spot has to be performed in 0.10 ms (row 10 of Table 5)

Acknowledgments